A&A 499, 439–453 (2009)
DOI: 10.1051/0004-6361/200911719

Astronomy & Astrophysics

Rise and fall of the X-ray flash 080330: an off-axis jet?⋆

C. Guidorzi[1,2,3], C. Clemens[4], S. Kobayashi[2], J. Granot[5], A. Melandri[2], P. D'Avanzo[1], N. P. M. Kuin[6], A. Klotz[7,8], J. P. U. Fynbo[9], S. Covino[1], J. Greiner[4], D. Malesani[9], J. Mao[1,10], C. G. Mundell[2], I. A. Steele[2], P. Jakobsson[11], R. Margutti[12,1], D. Bersier[2], S. Campana[1], G. Chincarini[12,1], V. D'Elia[13], D. Fugazza[1], F. Genet[5], A. Gomboc[14], T. Krühler[4], A. Küpcü Yoldaş[4], A. Moretti[1], C. J. Mottram[2], P. T. O'Brien[15], R. J. Smith[2], G. Szokoly[4], G. Tagliaferri[1], N. R. Tanvir[15], and N. Gehrels[16]

[1] INAF – Osservatorio Astronomico di Brera, via E. Bianchi 46, 23807 Merate (LC), Italy
e-mail: guidorzi@fe.infn.it
[2] Astrophysics Research Institute, Liverpool John Moores University, Twelve Quays House, Birkenhead CH41 1LD, UK
[3] Dipartimento di Fisica, Università di Ferrara, via Saragat 1, 44100 Ferrara, Italy
[4] Max-Planck-Institut für extraterrestrische Physik, 85740 Garching, Germany
[5] Centre for Astrophysics Research, University of Hertfordshire, College Lane, Hatfield, Herts AL10 9AB, UK
[6] Mullard Space Science Laboratory/UCL, Holmbury St Mary, Dorking, Surrey RH5 6NT, UK
[7] Observatoire de Haute-Provence, 04870 Saint-Michel l'Observatoire, France
[8] CESR, Observatoire Midi-Pyrénées, CNRS, Université de Toulouse, BP 4346, 31028 Toulouse Cedex 04, France
[9] Dark Cosmology Centre, Niels Bohr Institute, University of Copenhagen, Juliane Maries vej 30, 2100 København Ø, Denmark
[10] Yunnan Observatory, National Astronomical Observatories, Chinese Academy of Sciences, PO Box 110, Kunming, Yunnan Province 650011, PR China
[11] Centre for Astrophysics and Cosmology, Science Institute, University of Iceland, Dunhagi 5, IS 107 Reykjavik, Iceland
[12] Dipartimento di Fisica, Università di Milano-Bicocca, piazza delle Scienze 3, 20126 Milano, Italy
[13] INAF – Osservatorio Astronomico di Roma, via Frascati 33, 00040 Monteporzio (RM), Italy
[14] Faculty of Mathematics and Physics, University of Ljubljana, Jadranska 19, 1000 Ljubljana, Slovenia
[15] Department of Physics and Astronomy, University of Leicester, Leicester LE1 7RH, UK
[16] NASA Goddard Space Flight Center, Greenbelt, MD 20771, USA

Received 24 January 2009 / Accepted 8 March 2009

ABSTRACT

Context. X-ray flashes (XRFs) are a class of gamma-ray bursts (GRBs) with a peak energy of the time-integrated νF_ν spectrum, $E_{\rm p}$, typically below 30 keV, whereas classical GRBs have $E_{\rm p}$ of a few hundreds of keV. Apart from $E_{\rm p}$ and the systematically lower luminosity, the properties of XRFs, such as their duration or spectral indices, are typical of the classical GRBs. Yet, the nature of XRFs and their differences from GRBs are not understood. In addition, there is no consensus on the interpretation of the shallow decay phase observed in most X-ray afterglows of both XRFs and GRBs.

Aims. We examine in detail the case of XRF 080330 discovered by Swift at redshift 1.51. This burst is representative of the XRF class and exhibits an X-ray shallow decay. The rich broadband (from NIR to UV) photometric data set we collected during this phase makes it an ideal candidate for testing the off-axis jet interpretation proposed to explain both the softness of XRFs and the shallow decay phase.

Methods. We present prompt γ-ray, early and late NIR/visible/UV and X-ray observations of the XRF 080330. We derive a spectral energy distribution from NIR to X-ray bands across the shallow/plateau phase and describe the temporal evolution of the multi-wavelength afterglow within the context of the standard afterglow model.

Results. The multiwavelength evolution of the afterglow is achromatic from $\sim 10^2$ s to $\sim 8 \times 10^4$ s. The energy spectrum from NIR to X-ray is reproduced well by a simple power-law, $F_\nu \propto \nu^{-\beta_{\rm ox}}$, with $\beta_{\rm ox} = 0.79 \pm 0.01$ and negligible rest-frame dust extinction. The light curve can be modelled by either a piecewise power-law or the combination of a smoothly broken power law with an initial rise up to ~600 s, a plateau lasting up to ~2 ks, followed by a gradual steepening to a power-law decay index of ~2 until 82 ks. At this point, a bump appears to be modelled well with a second component, while the corresponding optical energy spectrum, $F_\nu \propto \nu^{-\beta_{\rm o}}$, reddens by $\Delta\beta_{\rm o} = 0.26 \pm 0.06$.

Conclusions. A single-component jet viewed off-axis can explain the light curve of XRF 080330, the late-time reddening being due to the reverse shock of an energy injection episode and its being an XRF. Other possibilities, such as the optical rise marking the pre-deceleration of the fireball within a wind environment, cannot be excluded definitely, but appear to be contrived. We exclude the possibility of a dust decreasing column density being swept up by the fireball as explaining the rise of the afterglow.

Key words. gamma rays: bursts – X-rays: individual: XRF 080330

1. Introduction

Time-integrated photon spectra of long gamma-ray bursts (GRBs) can be adequately fitted with a smoothly broken power-law (Band et al. 1993), whose low-energy and high-energy indices, $\alpha_{\rm B}$ and $\beta_{\rm B}$, have median values of −1 and −2.3, respectively (Preece et al. 2000; Kaneko et al. 2006). The corresponding νF_ν spectrum peaks at $E_{\rm p}$, the so-called peak energy, whose rest-frame value is found to correlate with other relevant observed intrinsic properties, such as the isotropic-equivalent

⋆ Table 5 is only available in electronic form at http://www.aanda.org

radiated γ-ray energy, $E_{\rm iso}$ (Amati et al. 2002), or its collimation-corrected value, E_γ (Ghirlanda et al. 2004). In the BATSE catalogue, the $E_{\rm p}$ distribution clusters around 300 keV with a ~100 keV width (Kaneko et al. 2006).

When observations of GRBs in softer energy bands than BATSE became available following the launches of BeppoSAX and HETE-2, a new class of soft GRBs with $E_{\rm p} \lesssim 30$ keV, so called X-ray flashes (XRFs), was soon discovered (Heise et al. 2001; Barraud et al. 2003). GRBs with intermediate softness, called X-ray rich (XRR) burst, were also observed with 30 keV $\lesssim E_{\rm p} \lesssim$ 100 keV (Sakamoto et al. 2005). These soft GRBs have almost identical temporal and spectral properties, apart from their systematically lower $E_{\rm p}$, to the classical GRBs both for the prompt (Frontera et al. 2000; Barraud et al. 2003; Amati et al. 2004) and, partially, the afterglow emission (Sakamoto et al. 2005; D'Alessio et al. 2006; Mangano et al. 2007). They were also found to obey the $E_{\rm p}$–$E_{\rm iso}$ correlation (Amati et al. 2007) discovered for classical GRBs, extending it all the way down to $E_{\rm p}$ values of a few keV and forming a continuum (Sakamoto et al. 2005). Like classical GRBs, XRFs have also been found to be associated with SNe (Campana et al. 2006; Pian et al. 2006) and therefore connected with the collapse of massive stars. The comparison between GRBs and XRFs also holds for the cases in which apparently no associated SN was found both for classical GRBs (e.g. Della Valle et al. 2006; Fynbo et al. 2006; Gal-Yam et al. 2006) and for XRFs (Levan et al. 2005).

A number of different models have been proposed in the literature to explain the nature of XRRs and XRFs (e.g., see the review of Zhang 2007): i) standard GRBs viewed well off the axis of the jet, which would explain the softness as being due to a larger viewing angle and a lower Doppler factor (Yamazaki et al. 2002; Granot et al. 2002, 2005); ii) two coaxial jets with different opening angles (wide and narrow), $\theta_{\rm w} > \theta_{\rm n}$, and viewed at an angle $\theta_{\rm v}$, $\theta_{\rm n} < \theta_{\rm v} < \theta_{\rm w}$ (Peng et al. 2005); iii) the "dirty fireball" model characterised by a small value of the bulk Lorentz factor caused by a relatively high baryon loading of the fireball (Dermer et al. 2000); iv) distribution of high Lorentz factors with low-contrast colliding shells (Mochkovitch et al. 2004). In the off-axis interpretation, a number of different models of the structure and opening angle of the jet have been proposed (e.g. Granot 2005; Donaghy 2006).

The advent of Swift (Gehrels et al. 2004) made it possible to collect a large sample of early X-ray afterglow light curves of GRBs. Concerning the XRRs and XRFs, the 15–150 keV energy band of the Swift Burst Alert Telescope (BAT; Barthelmy et al. 2005) and its relatively large effective area still allow us to detect them, although those with $E_{\rm p}$ of a few keV are less likely to be detected than by the BeppoSAX and HETE-2 instruments (Sakamoto et al. 2008). Thanks to Swift, it is possible to study the early X-ray afterglow properties of these soft events. Like hard GRBs, XRFs also occasionally exhibit X-ray flares (Romano et al. 2006). Sakamoto et al. (2008) analysed a sample of XRFs, XRRs and classical GRBs detected with Swift and found evidence of an average X-ray afterglow luminosity of XRFs being roughly half that of classical GRBs and some differences between the average X-ray afterglow light curves.

An unexpected discovery by Swift was the shallow decay phase experienced by most of X-ray afterglows between a few 10^2 s and 10^3–10^4 s after the trigger time (Tagliaferri et al. 2005; Nousek et al. 2006; Zhang et al. 2006). Several interpretations have been proposed (e.g., see Ghisellini et al. 2009 for a brief review). Some invoke continuous energy injection into the fireball shock front by means of refreshed shocks (Nousek et al. 2006; Zhang et al. 2006), depending on the progenitor period of activity, a long- or short-lived powering mechanism, either in the form of a prolonged, continuous energy release ($L(t) \propto t^{-q}$), or via discrete shells whose Γ distribution is a steep power-law. For instance, in the cases of GRB 050801 and GRB 070110, a newly born millisecond magnetar was suggested to power the flat decay observed in the optical and X-ray bands (De Pasquale et al. 2007; Troja et al. 2007). Alternatively, geometrical models interpret the shallow decay as the delayed onset of the afterglow observed from viewing angles outside the edge of a jet (Granot et al. 2002; Salmonson 2003; Granot 2005; Eichler & Granot 2006). Other models invoke two-component jets viewed off the axis of the narrow component, which have also been invoked to explain the late-time observations of GRB 030329 (Berger et al. 2003). This model would explain, in particular, the initial flat decay observed in XRF 030723, dominated by the wide component, followed by a late rebrightening peaking at ~16 days, which is interpreted to represent the deceleration and lateral expansion of the narrow component (Huang et al. 2004; Butler et al. 2005), although alternative explanations of this in terms of a SN have also been proposed (Fynbo et al. 2004; Tominaga et al. 2004).

Other models explain the shallow decay being caused by a temporal evolution in the fireball micro-physical parameters (Ioka et al. 2006; Granot et al. 2006), scattering by dust located in the circumburst medium (Shao & Dai 2007), "late prompt" activity of the inner engine, which sustains a prolonged emission of progressively lower power and Lorentz factor shells and radiate at the same distance as the prompt emission (Ghisellini et al. 2007, 2009), a dominating reverse shock in the X-ray band propagating through late shells with small Lorentz factors (Genet et al. 2007; Uhm & Beloborodov 2007). Yamazaki (2009) proposed that the plateau and the following standard decay phases are an artifact of the choice of t_0, provided that the engine activity begins before the trigger time by ~10^3–10^4 s.

XRF 080330 was promptly discovered by the Swift-BAT and automatically targeted by the X-Ray Telescope (XRT; Burrows et al. 2005) and the Ultraviolet/Optical Telescope (UVOT; Roming et al. 2005) as shown in Fig. 3. In this work, we present a detailed analysis of the Swift data, from the prompt γ-ray emission to the X-ray and optical afterglow and combine it with the extensive multi-filter data set collected from the ground, which includes broad-band data, from NIR to UV wavelengths, and spans time intervals from one minute to ~3 day post burst. The main properties exhibited by XRF 080330 are the rise of the optical afterglow until ~300 s, followed by a shallow decay that is also present in the X-ray, after which it gradually steepens and exhibits either a possible late-time (~10^5 s) brightening (Fig. 5) or a sharp break (Fig. 4). The richness of the multiwavelength data collected throughout the rise-flat top-steep decay allows us to constrain the broad-band energy spectrum of the shallow decay phase as well as its spectral evolution. Moreover, it is possible to constrain the optical flux extinction due to dust along the line of sight and, in particular, near the progenitor. This GRB is a good benchmark for proposed models of XRF sources and illustrates their link with classical GRBs in terms of their common properties, such as the flat decay phase.

The paper is organised as follows. Sections 2 and 3 report the observations, data reduction, and analysis. We report our multiwavelength combined analysis in Sect. 4. In Sect. 5, we discuss our results in the light of the models proposed in the literature, and Sect. 6 presents our conclusions.

Throughout the paper, times are given relative to the BAT trigger time. The convention $F(\nu, t) \propto \nu^{-\beta} t^{-\alpha}$ is followed, where the spectral index β is related to the photon index $\Gamma = \beta + 1$.

We adopted the standard cosmology: $H_0 = 70$ km s^{-1} Mpc^{-1}, $\Omega_\Lambda = 0.7$, $\Omega_M = 0.3$.

All quoted errors are given at 90% confidence level for one interesting parameter ($\Delta\chi^2 = 2.706$), unless stated otherwise.

2. Observations

XRF 080330 triggered the Swift-BAT on 2008 March 30 at 03:41:16 UT. The γ-ray prompt emission in the 15–150 keV energy band consisted of a multiple–peak structure with a duration of about 60 s (Mao et al. 2008a). An uncatalogued, bright, and fading X-ray source was promptly identified by XRT. From the initial 100-s finding chart taken with the UVOT telescope in the White filter from 82 s, the optical counterpart was initially localised at RA = $11^h17^m04^s.51$, Dec = $+30°37'22''.1$ (J2000) with an error radius of $1''.0$ (1σ; Mao et al. 2008a). During the observations, the Swift star trackers failed to maintain a proper lock resulting in a drift, which affected the observations and accuracy of early reports. We finally refined the position by cross-correlating the UVOT field with the USNO–B1 catalogue to be RA = $11^h17^m04^s.52$, Dec = $+30°37'23''.5$ (J2000), with an error radius of $0''.3$ (1σ; Mao et al. 2008b), which is consistent with the position derived from ground telescopes (e.g., PAIRITEL, Bloom & Starr 2008).

The Télescopes à Action Rapide pour les Objets Transitoires (TAROT; Klotz et al. 2008c) began observing at 20.4 s (4.5 s after the notice) and discovered independently the optical counterpart during the rise with $R \sim 16.8$ at 300 s (Klotz et al. 2008a). TAROT continued to observe until the dawn at 1.4 ks (Klotz et al. 2008b).

The Rapid Eye Mount[1] (REM; Zerbi et al. 2001) telescope reacted promptly and began observing at 55 s, detecting the optical afterglow in R band (D'Avanzo et al. 2008). The optical counterpart was also promptly detected by other robotic telescopes, such as ROTSE–IIIb (Schaefer et al. 2008; Yuan et al. 2008), PROMPT (Schubel et al. 2008), and RAPTOR; the last telescope in particular observed a ~10-s long optical flash of $R = 17.46 \pm 0.22$ at 60 s that was contemporaneous with the last γ-ray pulse (Wren et al. 2008).

The Liverpool Telescope (LT) began observing at 181 s. The optical afterglow was automatically identified by the LT-TRAP GRB pipeline (Guidorzi et al. 2006) with $r' \sim 17.3$ (Gomboc et al. 2008a), which triggered the multi-colour imaging observing mode for the $g'r'i'$ filters, which lasted until the dawn at 4.9 ks. The Faulkes Telescope North (FTN) observations of XRF 080330 were carried out from 8.4 to 9.1 h and again from 31.8 to 33.9 h with deep r' and i' filter exposures. The Gamma-Ray Burst Optical and Near-Infrared Detector (GROND; Greiner et al. 2008) started simultaneous observations in $g'r'i'z'JHK$ filters of the field of GRB 080330 at 3.1 min and detected the afterglow with $J = 15.92 \pm 0.04$ and $H = 15.46 \pm 0.11$ from the first 240 s of effective exposure (Clemens et al. 2008). A spectrum of XRF 080330 was acquired at 46 min with the Nordic Optical Telescope (NOT). The identification of absorption features allowed us to measure its redshift, which turned out to be $z = 1.51$ (Malesani et al. 2008). This was soon confirmed by the spectra taken with the Hobby-Eberly Telescope (Cucchiara & Fox 2008).

The Galactic reddening along the line of sight to the GRB is $E_{B-V} = 0.017$ (Schlegel et al. 1998). The corresponding extinction in each filter was estimated by using the NASA/IPAC Extragalactic Database extinction calculator[2]: $A_{UVW1} = 0.120$, $A_U = 0.090$, $A_B = 0.071$, $A_g = 0.064$, $A_V = 0.055$, $A_r = 0.047$, $A_R = 0.044$, $A_I = 0.032$, $A_i = 0.035$, $A_z = 0.022$, $A_J = 0.015$, $A_H = 0.010$, $A_K = 0.006$.

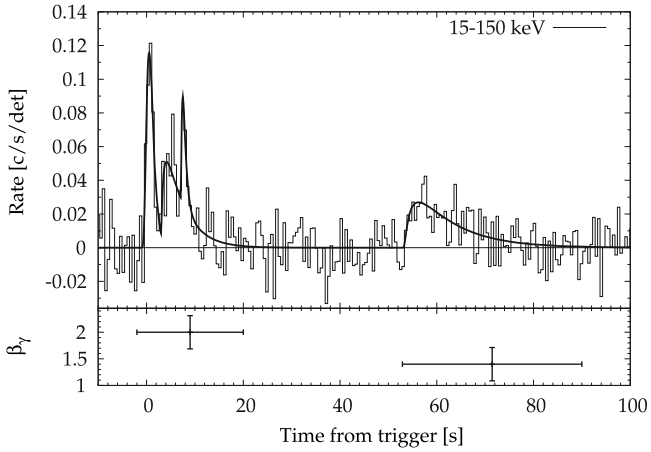

Fig. 1. *Top panel*: 15–150 keV BAT mask-weighted light curve (binning time of 0.512 s). The thick solid line shows the result of fitting the profile with four pulses modelled with Norris profiles (Norris et al. 2005). *Bottom panel*: spectral index β_γ as a function of time.

3. Data reduction and analysis

3.1. Gamma-ray data

The BAT data were processed with the `heasoft` package (v.6.4) adopting the ground-refined coordinates provided by the BAT team (Markwardt et al. 2008). The BAT detector quality map was obtained by processing the nearest-in-time enable/disable map of the detectors.

The top panel of Fig. 1 shows the 15–150 keV mask-weighted light curve of XRF 080330 as recorded by BAT, expressed as counts per second per fully illuminated detector for an equivalent on-axis source. The solid line displayed in Fig. 1 corresponds to the result of fitting the profile from −1.2 to 100 s with a combination of four pulses (Markwardt et al. 2008) as modelled by Norris et al. (2005; hereafter N05 model). Table 1 reports the corresponding derived parameters: t_p (peak time), A (15–150 keV peak flux), τ_r (rise time), τ_d (decay time), w (pulse width), k (pulse asymmetry), and the model fluence in the 15–150 keV band. The goodness of the fit is χ^2/d.o.f. = 375/379. Parameter uncertainties were derived by propagation starting from the best-fit parameters and taking into account their covariance. We tried to apply the same analysis to the light curves of the resolved energy channels to investigate temporal lags and, more generally, the dependence of the parameters on energy; however, because of the faintness and softness of the signal, we were unable to constrain the parameters in a useful way.

The energy spectra in the 15–150 keV band were, in addition, extracted using the tool `batbinevt`. We applied all the required corrections by updating them with `batupdatephakw` and generated the detector response matrices using `batdrmgen`. We then used `batphasyserr` to account for the BAT systematics as a function of energy. We finally divided the spectra into energy channels by imposing a 3σ (or 2-σ when the S/N was too low) threshold on each grouped channel. We fitted the resulting photon spectra, $\Phi(E)$ (ph cm^{-2} s^{-1} keV^{-1}) with a power

[1] http://www.rem.inaf.it/

[2] http://nedwww.ipac.caltech.edu/forms/calculator.html

Table 1. Best-fit model parameters of the 15–150 keV profile decomposed into four pulses using the model by Norris et al. (2005). Uncertainties are 1σ.

Pulse	t_p (s)	A (10^{-8} erg cm^{-2} s^{-1})	τ_r (s)	τ_d (s)	w (s)	k	Fluence (10^{-8} erg cm^{-2})
1	0.5 ± 0.2	4.6 ± 0.6	0.79 ± 0.18	1.30 ± 0.26	2.09 ± 0.29	0.24 ± 0.16	8.6 ± 1.0
2	4.2 ± 0.6	2.0 ± 0.3	1.04 ± 0.64	4.71 ± 1.30	5.75 ± 1.44	0.64 ± 0.20	10.8 ± 1.9
3	7.5 ± 0.2	2.5 ± 0.7	0.32 ± 0.19	0.84 ± 0.43	1.16 ± 0.46	0.45 ± 0.32	2.7 ± 0.8
4	56.2 ± 1.2	1.3 ± 0.2	2.52 ± 1.26	10.5 ± 2.3	13.0 ± 2.4	0.61 ± 0.18	15.5 ± 2.3

Table 2. Best-fit model parameters of the 15–150 keV and of the 0.3–10 keV spectra of the γ-ray prompt and X-ray afterglow measured with BAT and XRT, respectively[a].

Interval	Energy band (keV)	Start time (s)	Stop time (s)	β	$N_{H,z}$ (10^{21} cm^{-2})	Mean flux (erg cm^{-2} s^{-1})	$A^b_{V,z}$	χ^2/d.o.f.
T_{90}	15–150	0.0	67.0	1.44 ± 0.46	–	$(3.3 \pm 0.8) \times 10^{-7}$	–	1.44/6
Total	15–150	−2.0	90.0	1.65 ± 0.51	–	$(3.6 \pm 0.8) \times 10^{-7}$	–	5.6/7
Pulses 1–3	15–150	−2.0	20.0	2.0 ± 0.5	–	$(2.2 \pm 0.5) \times 10^{-7}$	–	1.82/7
Pulse 4	15–150	52.9	90.0	1.4 ± 0.5	–	$(1.4 \pm 0.5) \times 10^{-7}$	–	5.8/5
Peak	15–150	0.384	0.832	1.1 ± 0.6	–	$(1.0 \pm 0.2)^c$	–	6.1/6
XRT-WT	0.3–10	77	134	$1.06^{+0.10}_{-0.09}$	<1.4	$(4.1 \pm 0.3) \times 10^{-10}$	–	28.3/31
Plateau	0.3–10	423	1507	$0.80^{+0.16}_{-0.15}$	$1.6^{+1.8}_{-1.5}$	$(2.3 \pm 0.3) \times 10^{-11}$	–	17.2/24
SED 2	opt-X	186.8	269.4	0.74 ± 0.03	[2.7]	–	<0.04	8.2/6
SED 3	opt–X	423	1507	0.79 ± 0.01	2.7 ± 0.8	–	<0.02	32/34
SED 4	opt	78 117	93 620	0.85 ± 0.30	–	–	$0.10^{+0.14}_{-0.06}$	3.4/4
SED 2	opt	186.8	269.4	0.61 ± 0.13	–	–	[0]	3.1/3
SED 3	opt	423	1507	0.74 ± 0.05	–	–	[0]	7.9/8
SED 4	opt	78 117	93 620	1.05 ± 0.06	–	–	[0]	4.8/5

[a] The model is an absorbed power law (`xspec` model: `pegpwrlw` for BAT and `wabs pow` for XRT data, respectively). Frozen values are reported among square brackets. SED modelling results are also reported, both derived for the broad band from optical to X-rays and optical points alone. The extinction is modelled with a SMC profile as parametrised by Pei (1992); [b] rest-frame extinction obtained by modelling the SED with an SMC profile as parametrised by Pei (1992); [c] peak photon flux in units of ph cm^{-2} s^{-1}.

law with pegged normalisation (`pegpwrlw` model under `xspec` v.11.3.2). We extracted several spectra for different time intervals: across the total interval of T_{90}, spanned by the bunch of the first three pulses, that of the fourth pulse alone, and that around the peak, determined on a minimum significance criterion. The results are reported in Table 2. The time-averaged spectral index is $\beta_\gamma = 1.65 \pm 0.51$ with a total fluence of $S(15{-}150\ \mathrm{keV}) = (3.6 \pm 0.8) \times 10^{-7}$ erg cm^{-2} and a 0.448-s peak photon flux of (1.0 ± 0.2) ph cm^{-2} s^{-1}, in agreement with previous results (Markwardt et al. 2008). The bottom panel of Fig. 1 shows marginal evidence of soft-to-hard evolution: β_γ passes from 2.0 ± 0.5 (first three pulses) to 1.4 ± 0.5 (fourth pulse).

Following Sakamoto et al. (2008), a GRB is classified as an XRR (XRF) depending on whether the fluence ratio $S(25{-}50\ \mathrm{keV})/S(50{-}100\ \mathrm{keV})$ is lower (greater) than 1.32. The fluence ratio of XRF 080330, $1.5^{+0.7}_{-0.3}$, implies that it is an XRF, although still compatible with being an XRR burst. Although we were unable to determine the peak energy of the time-integrated νF_ν spectrum from BAT data alone, we attempted to reproduce the spectrum with a smoothed broken power-law model (Band et al. 1993) by fixing the low-energy index α_B to -1 (Kaneko et al. 2006), given that $\Gamma = \beta_\gamma + 1 > 2$ and this parameter is probably dominated by the high-energy index β_B. This way, we derived the constraint $E_p < 35$ keV, in agreement with the upper limit to the rest-frame (intrinsic) value, $E_{p,i} = E_p(1+z) < 88$ keV, obtained by Rossi et al. (2008).

Sakamoto et al. (2009) calibrated a method for estimating E_p from the Γ_γ measured from BAT data, provided that $1.3 < \Gamma < 2.3$. In the case of XRF 080330, the confidence interval on Γ, 2.65 ± 0.51, marginally overlaps with the allowed range; however, since E_p is anticorrelated with Γ and the lower limit to Γ is within the usable range, we can derive an upper limit to E_p from the relation of Sakamoto et al. (2009), which turns out to be 30 keV, in agreement with our previous value. These results are fully consistent with a previous preliminary analysis (Markwardt et al. 2008).

We constrained E_{iso} in the rest-frame $1{-}10^4$ keV band using the upper limit to E_p of 35 keV. Following the prescriptions by Amati et al. (2002) and Ghirlanda et al. (2004), we found that $E_{iso} < 2.2 \times 10^{52}$ erg. Combined with $E_{p,i} < 88$ keV, this places XRF 080330 in the $E_{p,i}$–E_{iso} space consistently with the Amati relation (Amati et al. 2002; Amati 2006).

3.2. X-ray data

The XRT data were processed using the `heasoft` package (v.6.4). We applied the task `xrtpipeline` (v.0.11.6) and in particular both its calibration and standard filtering, and screening criteria. Data between 77 and 134 s were acquired in Windowed Timing (WT) mode and subsequently gathered data in Photon Counting (PC) mode due to the faintness of the source. Events with grades 0–2 and 0–12 were selected for the two modes, respectively. XRT observations continued until 5.9×10^5 s, with a total net exposure time of 30.6 ks. The XRT analysis was performed in the 0.3–10 keV energy band.

Source photons were extracted from WT mode data in a rectangular region 40 pixels along the image strip (20 pixel wide)

centred on the source, whereas the background photons were extracted from an equally-sized region with no sources.

Firstly, we extracted the first orbit PC data from 136 s to 331 s, where the point spread function (PSF) of the source looked unaffected by the spacecraft drifting, and extracted the refined position of RA = $11^h17^m04\overset{s}{.}68$, Dec = $+30°37'24\overset{''}{.}8$ (J2000), with an error radius of 4.0 arcsec (Mao & Guidorzi 2008). We corrected these data for pile-up by extracting source photons from an annular region centred on the above position of inner and outer radii of 4 and 30 pixels (1 pixel = $2\overset{''}{.}36$), respectively. The background was estimated from a three-circle region with a total area of 30.3×10^3 pixel^2 away from any source present in the field. Finally, we re-extracted the source photons over the entire first orbit within a larger circular region centred on the same position and with a radius of 40 pixels, to compensate for the drifting. The light curve of the full first orbit data (PC mode) was then corrected so as to match the previous one correctly produced in the 136–331 s subinterval.

The resulting 0.3–10 keV light curve is shown in Fig. 3 (black empty triangles). It was binned so as to achieve a minimum signal-to-noise ratio (SNR) of 3. The data acquired in subsequent orbits were not of sufficiently high quality to achieve a significant detection and only a 3σ upper limit was obtained.

The X-ray curve could be fitted by a broken power-law with the parameters $\alpha_{x,1} = 4.8 \pm 0.4$, $t_b = 163^{+9}_{-10}$ s and $\alpha_{x,2} = 0.26 \pm 0.10$ (χ^2/d.o.f. = 66/70). The last point is a 3-σ upper limit which clearly requires a further break. We set a lower limit to $\alpha_{x,3}$ by connecting the end of first orbit data with the late upper limit under the assumption that the second break occurred at the beginning of the data gap. This implies that $\alpha_{x,3} > 1.3$ ($\geq 3\sigma$ confidence). The later the second break time, the steeper the final decay became.

We extracted 0.3–10 keV spectra for two different time intervals: i) "XRT-WT" interval, from 77 to 134 s (WT mode), corresponding to the initial steep decay; and ii) "plateau" interval, from 423 to 1507 s (PC mode) corresponding to the following flat-decay (or "plateau") phase. Source and background spectra were extracted from the same regions used for the light curve for the corresponding time intervals and modes. The ancillary response files were generated using the task `xrtmkarf`. Spectral channels were grouped so as to have at least 20 counts per bin. Spectral fitting was performed with `xspec` (v. 11.3.2).

We modelled both spectra with a photoelectrically absorbed power law (model `wabs·zwabs·pow`), adopting the photoelectric cross-section of Morrison & McCammon (1983). The first column density was frozen to the weighted average Galactic value along the line of sight to the GRB, $N_H^{(Gal)} = 1.23 \times 10^{20}$ cm^{-2} (Kalberla et al. 2005), while the second rest-frame column density, $N_{H,z}$, was allowed to vary. During the steep decay, we found no evidence of significant rest-frame absorption, with a 90% confidence limit of $N_{H,z} < 1.4 \times 10^{21}$ cm^{-2}, while in the plateau spectrum, we found only marginal evidence of absorption, $N_{H,z} = 1.6^{+1.8}_{-1.5} \times 10^{21}$ cm^{-2}. The spectral index, β_x, varies from $1.06^{+0.10}_{-0.09}$ to $0.80^{+0.16}_{-0.15}$, the significance of this change being $\sim 2.3\sigma$. The best-fit parameters are reported in Table 2.

3.3. Near–UV/Visible UVOT data

The Swift UVOT instrument started observing on 2008 March 30 at 03:42:19 UT, 63 s after the BAT trigger, with a 9.37-s settling exposure. Since the detectors are powered up during this exposure, the effective exposure time may be less than reported. We checked the brightness in this exposure with later exposures, to confirm that no correction was needed. The first 99.7-s finding chart exposure started at 03:42:39 UT in the white filter in event mode followed by a 399.8-s exposure in the V filter, also in event mode. Because of the loss of lock by the spacecraft star trackers, the attitude information was incorrect. To process the data, `xselect` was used to extract images for short time intervals. The length of the interval was chosen to be short enough for the drift of the spacecraft to be mostly within 7″, and at most 14″, but long enough to derive a reasonably accurate measurement. A source region was placed over the position of the source, consistency checks being made with the position of nearby stars, and the magnitudes were determined using the ftool `uvotevtlc`. In most cases, an aperture with a radius of 5″ was used, and three measurements used a slightly larger aperture. No aperture correction was made, since the source shape in those cases was very elongated. The measured magnitudes were converted back to the original count rates, using the UVOT calibration (Poole et al. 2008). These were subsequently converted to fluxes using the method of Poole et al. (2008), but for an incident power-law spectrum with $\beta = 0.8$ and for a redshift $z = 1.51$.

3.4. NIR/Visible ground-based data

Robotically triggered observations with the LT began at 181 s leading to the automatic identification by the GRB pipeline LT-TRAP (Guidorzi et al. 2006) of the optical afterglow at the position RA = $11^h17^m04\overset{s}{.}48$, Dec = $+30°37'23\overset{''}{.}8$ (J2000; 1σ error radius of 0.2 arcsec). This is consistent within 1.6σ with the refined UVOT position. The afterglow was seen during the end of the rise with $r' = 17.3 \pm 0.1$ and the subsequent decay (Gomboc et al. 2008a). Following two initial sequences of 3×10 s each in the r' filter during the detection mode (DM), the multi-colour imaging observing mode (MCIM) in the $g'r'i'$ filters was automatically selected. Observations carried on until 4.9 ks.

The FTN observations of XRF 080330 were carried out between 8.4 and 9.1 h and again from 31.8 to 33.9 h with deep r' and i' filter exposures as part of the *RoboNet 1.0* project[3] (Gomboc et al. 2006).

Calibration was performed by comparing with the magnitudes of five non-saturated field stars with preburst SDSS photometry (Cool et al. 2008), by adopting their PSF to adjust the zero point of the single images. Photometry was carried out using the Starlink GAIA software. Magnitudes were converted into flux densities (mJy) following Fukugita et al. (1996). Results are reported in Table 5.

Optical R-band observations of the afterglow of GRB 080330 were carried out with the REM telescope equipped with the ROSS optical spectrograph/imager on 2008 March 30, starting about 55 s after the burst (D'Avanzo et al. 2008). We collected 38 images with typical exposures times of 30, 60, and 120 s, covering a time interval of about 0.5 h. Image reduction was carried out by following the standard procedures of subtraction of an averaged bias frame and division by a normalised flat frame. The astrometry was fitted using the USNOB1.0[4] catalogue. We grouped our images into 18 bins to increase the signal-to-noise ratio (SNR), and performed aperture photometry with the SExtractor package (Bertin & Arnouts 1996) for all the objects in the field. To minimise our systematical errors, we performed differential photometry

[3] http://www.astro.livjm.ac.uk/RoboNet/
[4] http://www.nofs.navy.mil/data/fchpix/

with respect to a selection of local isolated and non-saturated standard stars.

The calibration of NOT images taken with the R filter was performed by comparing with the converted magnitudes in the R-band of the selected set of stars used to calibrate the LT and GROND images in the SDSS passbands. We transformed the r' and i' magnitudes of the calibration stars (Cool et al. 2008) into R and I magnitude following the filter transformations of Krisciunas et al. (1998).

Hereafter, the magnitudes shown are not corrected for Galactic extinction, whilst fluxes as well as all the best-fit models are. When the models are plotted together with magnitudes, the correction for Galactic extinction is removed from the models.

3.5. Spectroscopy

Starting at ≈46 min, we obtained a 1800 s spectrum with a low resolution grism and a 1.3-arcsec-wide slit covering the spectral range from about 3500 to 9000 Å at a resolution of 14 Å with the NOT (Fig. 2). The airmass was about 1.8 at the start of the observations. The spectroscopic data were reduced using standard methods for bias subtraction, flat-fielding, and wavelength calibration using an helium-neon arc spectrum. The rms of the residuals in the wavelength calibration were about 0.3 Å. The spectrum was flux-calibrated using an observation with the same setup of the spectrophotometric standard star HD93521. Table 6 reports the identified lines.

4. Multi-wavelength combined analysis

4.1. Panchromatic light curve

Figure 3 displays the light curves of the prompt emission (15–150 keV) and the 0.3–10 keV and NIR/visible/UV afterglow derived from our data sets, plus some points taken from RAPTOR (Wren et al. 2008). High-energy fluxes (magnitudes) are referred to along the right-hand (left-hand) y-axis. First of all, we noted that the peak time of the last γ-ray pulse (Table 1) is contemporaneous with the optical flash detected by RAPTOR, reported to occur at 58.9 ± 2.5 s (Wren et al. 2008).

The initial steep decay observed by XRT is a smooth continuation of the last γ-ray pulse, and is thus the tail of the prompt GRB emission and likely to correspond to its high-latitude emission. Most notably, during the X-ray steep decay the optical flux is seen to rise up to ∼300 s and finally a simultaneous plateau is reached at both energy bands, lasting up to ∼1500 s, when the X-ray observations stopped. This strongly suggests that the plateau is emission from a region that is physically distinct from that responsible for the prompt emission and its tail (the rapid decay phase).

As discussed in Sect. 4.2, the afterglow does not show evidence of spectral evolution throughout the observations, except for late epochs ($t \sim 10^5$ s) when there is evidence for reddening. The achromatic nature of the afterglow light curve allows us to perform a multiwavelength simultaneous fit of twelve light curves, where only the normalisations are allowed to vary independently from each other. We consider data for all the available passbands, K, H, J, z', i', r', V, g', B, U, $UWV1$, and X-ray. The X-ray curve is fitted from 300 s onward, so as to exclude the initial steep decay. Hereafter, we present two alternative combinations of models, both providing a reasonable description of the flux temporal evolution. In both cases we had to apply a 2% systematic error to all of the measured uncertainties to account for some residual variability with respect to the models, to derive acceptable χ^2 values and correspondingly acceptable parameter uncertainties.

4.1.1. Multiple smoothly broken power law

An accurate description of the light curves is provided by a multiple broken power law (Fig. 4). This has the advantage of a more straightforward interpretation in terms of the standard fireball evolution model due to synchrotron emission. We started from the parametrisation by Beuermann et al. (1999) and added two further breaks to finally provide a sufficiently detailed description. The fitting function is given by Eq. (1).

$$F(t) = \frac{F_0}{\left[(t/t_{b1})^{n\,\alpha_1} + (t/t_{b1})^{n\,\alpha_2} + (t/t_{b2})^{n\,\alpha_3} + (t/t_{b3})^{n\,\alpha_4}\right]^{1/n}} \cdot \quad (1)$$

The free parameters are the normalisation constant (different for each curve), F_0, three break-time constants, $t_{\rm bi}$ ($i = 1, 2, 3$), four power-law indices, $\alpha_1 < \alpha_2 < \alpha_3 < \alpha_4$, and the smoothness n. Apart from the normalisations, all the curves share the same parameters. Overall, the number of free parameters and the degrees of freedom (d.o.f.) are 20 and 184, respectively.

Equation (1) looks like a piecewise power law only in the regime $t_{b1} \ll t_{b2} \ll t_{b3}$, where each individual term dominates at the separate epochs. The light curve of XRF 080330 is reproduced well in this case, as proven by the best-fit model results (first line of Table 3) and shown in Fig. 4. The effective break times, $t_{b1,\rm eff}$, $t_{b2,\rm eff}$, $t_{b3,\rm eff}$, i.e., the times at which the model in Eq. (1) changes the power-law regime, are simply given by $t_{b1,\rm eff} = t_{b1}$, $t_{b2,\rm eff} = (t_{b1}^{\alpha_2}/t_{b2}^{\alpha_3})^{1/(\alpha_2-\alpha_3)}$, $t_{b3,\rm eff} = (t_{b2}^{\alpha_3}/t_{b3}^{\alpha_4})^{1/(\alpha_3-\alpha_4)}$.

The goodness of the fit in terms of χ^2/d.o.f. is 212/184, corresponding to a non-rejectable P-value of 7.7%. The normalisation constants for the different bands are (in μJy) $F_K = 1077^{+54}_{-59}$, $F_H = 942^{+45}_{-50}$, $F_J = 769^{+40}_{-44}$, $F_z = 643^{+26}_{-30}$, $F_i = 554^{+19}_{-25}$, $F_r = 464^{+16}_{-21}$, $F_V = 418^{+34}_{-33}$, $F_g = 362^{+12}_{-16}$, $F_B = 362 \pm 68$, $F_U = 277 \pm 45$, and $F_{UVW1} = 129 \pm 52$, while the X-ray normalisation, expressed in flux units in the 0.3–10 keV band instead of flux density, is $F_{\rm x} = (3.7 \pm 0.3) \times 10^{-11}$ erg cm^{-2} s^{-1}. The effective break times are found be $t_{b1,\rm eff} = 317$ s, $t_{b2,\rm eff} = 1850$ s, and $t_{b3,\rm eff} = 82.4$ ks, respectively.

The bottom panel of Fig. 4 shows the residuals of the r' curve with respect to the model; the displayed uncertainties do not include the 2% systematic offset error added by the fitting procedure. We note that between 6 and 7×10^3 s the model overpredicts the flux by 2–4σ with respect to the measured values, corresponding to a ∼0.1 mag difference. However, the later points seem to rule out a steeper decay than the modelled one. Alternatively, one might interpret this as being indicative of a steeper decay followed by a second component that hence causes a late flux enhancement. This possibility motivated us to provide the alternative description described in Sect. 4.1.2.

4.1.2. A two-component model: late-time brightening

In Fig. 5, we modelled the first part ($t < 10^4$ s) of the light curve with a simple smoothly broken power law with a single break time, t_{b1}, and two power-law indices, α_1 (α_2), dominating at $t \ll t_{b1}$ ($t \gg t_{b1}$). To model the later data points, we had to add an additional component. A Lorentzian proved successful

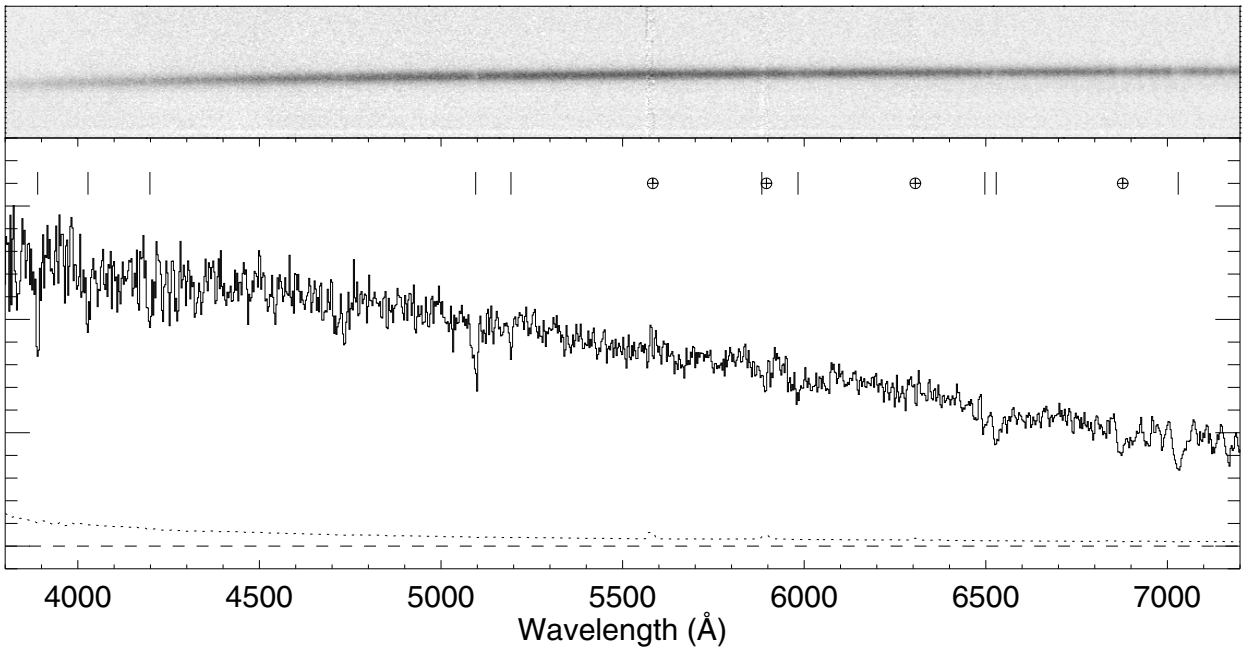

Fig. 2. The NOT spectrum of the afterglow taken at 46 min post-burst. The tick marks and Earth symbols show the absorption features (Table 6) and telluric lines, respectively. The dotted line shows the error spectrum.

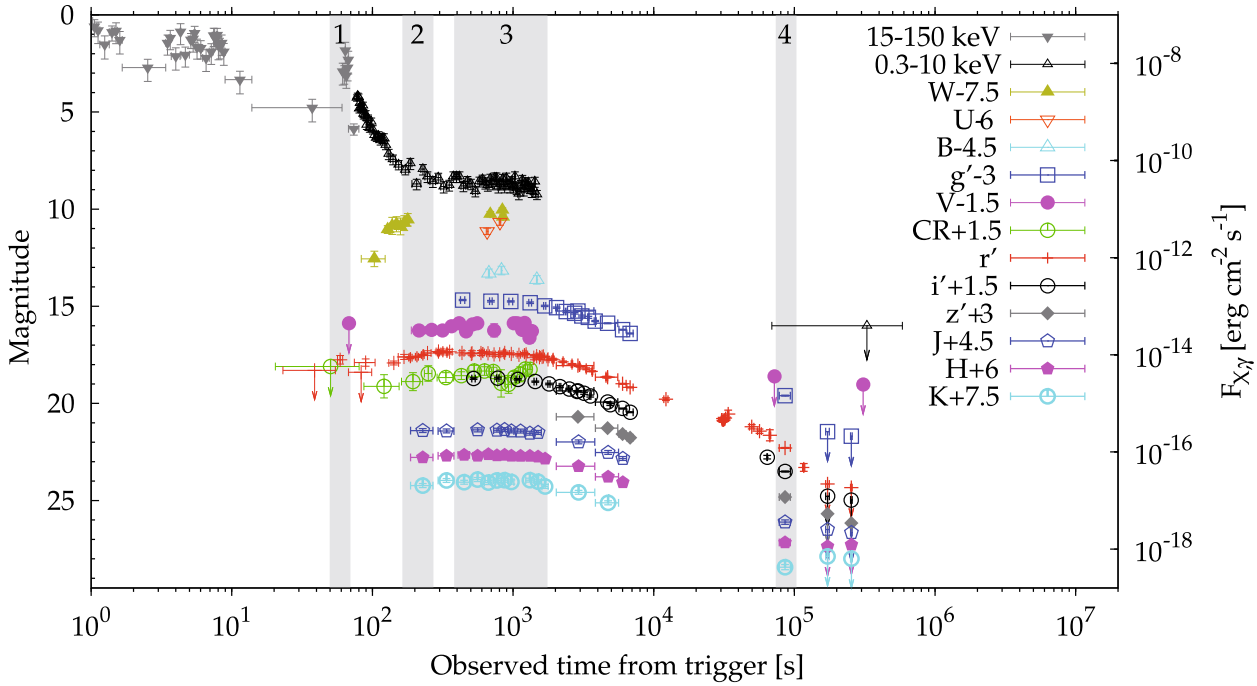

Fig. 3. Panchromatic light curve of the prompt (BAT, 15–150 keV), X-ray (XRT, 0.3–10 keV) and NIR/visible/UV (FTN, GROND, LT, NOT, REM, TAROT, UVOT–W) afterglow of XRF 080330. Magnitudes (high-energy fluxes) are referred to along the left-hand (right-hand) y-axis. RAPTOR points were taken from Wren et al. (2008) and shifted by 0.3 mag to match contemporaneous r' points. The shaded bands indicate the four intervals where we computed the SEDs.

Table 3. Best-fit model parameters of the multiwavelength fitting procedure of the afterglow light curves.

α_1	t_{b1} (s)	α_2	t_{b2} (s)	α_3	t_{b3} (ks)	α_4	n	t_c (ks)	t_w (ks)	$F_{L,r}$ (μJy)	χ^2/d.o.f.
$-0.56^{+0.24}_{-0.33}$	317^{+151}_{-76}	$0.15^{+0.09}_{-0.07}$	1456^{+67}_{-46}	1.08 ± 0.02	$23.8^{+3.2}_{-3.1}$	$3.51^{+0.37}_{-0.34}$	$5.4^{+1.9}_{-1.3}$	–	–	–	212/184
$-0.38^{+0.22}_{-0.23}$	2480^{+1420}_{-900}	$2.02^{+0.85}_{-0.75}$	–	–	–	–	$0.49^{+0.61}_{-0.28}$	$34.4^{+10.6}_{-8.1}$	$72.7^{+14.6}_{-12.2}$	$11.9^{+3.5}_{-2.7}$	187/185

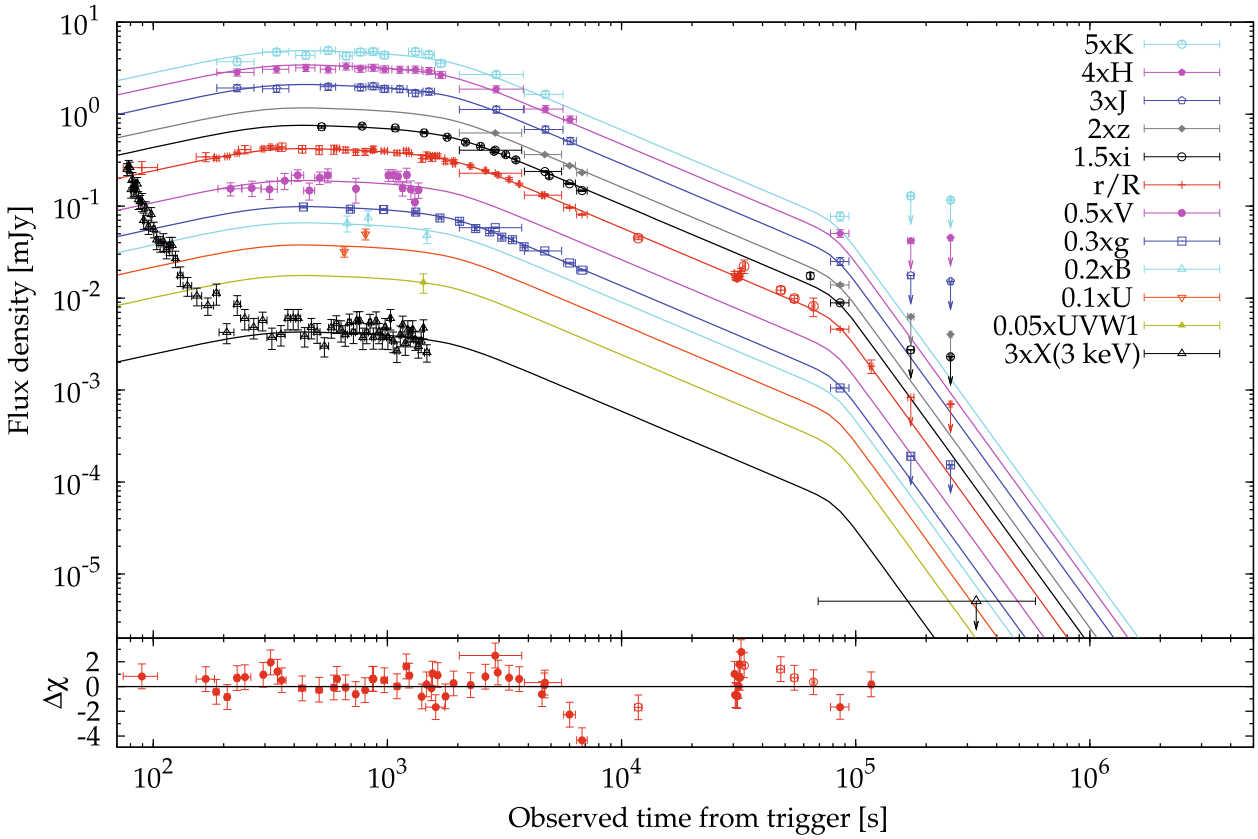

Fig. 4. *Top panel*: NIR/visible/UV/X-ray light curves expressed in flux densities units, after correction for Galactic extinction. The effective wavelength decreases *from top to bottom*, from K filter all the way down to X-rays. Red empty circles are public data points from literature (Im et al. 2008; Wang et al. 2008; Sergeev et al. 2008; Moskvitin et al. 2008). Upper limits are 3σ. The solid lines show the same model of a multiple smoothly broken power-law obtained by fitting all the curves simultaneously, allowing for different normalisations but with the same fit parameters. *Bottom panel*: residuals of the r' curve with respect to the corresponding model.

in this respect, so that the complete model used is given by the following equation.

$$F(t) = \frac{F_{0,r}}{\left[(t/t_{b1})^{n\,\alpha_1} + (t/t_{b1})^{n\,\alpha_2}\right]^{1/n}} + \frac{F_{\rm L,r}}{1 + \left[2\,(t - t_{\rm c})\,/t_{\rm w}\right]^2}\,. \qquad (2)$$

This was used to fit the r' curve. The free parameters are the normalisation constant, $F_{0,r}$, the break time, t_{b1}, two power-law indices, α_1 and α_2, the smoothness n, the Lorentzian normalisation, $F_{\rm L,r}$, the peak time, $t_{\rm c}$ and its width, $t_{\rm w}$. The time-integrated flux density of the latter component is $\pi\,F_{\rm L,r}\,t_{\rm w}/2$. The two terms of Eq. (2) peak at $t_{p1} = t_{b1}(-\alpha_1/\alpha_2)^{1/[n(\alpha_2-\alpha_1)]}$ and $t_{p2} = t_{\rm c}$, respectively. Each of the light curves of the remaining filters were fitted with a free scaling factor with respect to the r' curve as modelled by Eq. (2). The number of free parameters and the d.o.f. equalled 19 and 185, respectively.

The best-fit model result is shown in Fig. 5, while the second line of Table 3 reports the corresponding best-fit model parameter values. The fit is good with χ^2/d.o.f. = 187/185. The scaling factors for the remaining bands are $f_K = 2.31 \pm 0.12$, $f_H = 2.03 \pm 0.10$, $f_J = 1.65 \pm 0.09$, $f_z = 1.40 \pm 0.04$, $f_i = 1.20 \pm 0.03$, $f_V = 0.90 \pm 0.08$, $f_g = 0.78 \pm 0.02$, $f_B = 0.77^{+0.19}_{-0.15}$, $f_U = 0.59^{+0.12}_{-0.10}$, and $f_{UVW1} = 0.28^{+0.17}_{-0.11}$, while the X-ray normalisation is still $F_{\rm x} = (3.7 \pm 0.3) \times 10^{-11}$ erg cm^{-2} s^{-1}. The two components peak at $t_{p1} = 600$ s and $t_{p2} = 34.4$ ks.

We also tried to model the second component with a rising and falling smoothly broken power law instead of a Lorentzian. However, this introduced too many free parameters, such as the slope of the rise, so unless one finds a reason to fix some of the parameters to specific values, fitting with this component can yield highly undetermined parameters.

4.2. Spectral energy distribution

Figure 7 displays four SEDs derived for as many different time intervals (see shaded bands in Fig. 3):

1. SED 1 includes the last γ-ray pulse and the optical flash detected by RAPTOR (Wren et al. 2008), around 60 s;
2. SED 2 corresponds to the final part of the optical rise, coinciding with the final part of the X-ray steep decay, spanning from 186.8 to 269.4 s;
3. SED 3 has the broadest wavelength coverage and corresponds to the plateau phase, from ~400 to ~1500 s.
4. SED 4 includes NIR/visible measurements around the possible late-time break in the light curve (Fig. 4), at ~10^5 s.

To construct SED 1, we adopted the RAPTOR measurement (Wren et al. 2008), a UVOT upper limit to the V band, and the BAT spectrum of the fourth pulse. Figure 6 displays the resulting SED: the solid line shows the best fit with a smoothed broken power law used to fit the high-energy photon spectra of the prompt emission of GRBs (Band et al. 1993). The best-fit model parameters are $\alpha_{\rm B} = -1.12$, $\beta_{\rm B} = -2.35$, and $E_{\rm p,i} = 71$ keV (χ^2/d.o.f. = 5.8/5), consistent with the limit to $E_{\rm p,i}$ derived in Sect. 3.1. The Band indices are photon indices, so the corresponding energy indices are 0.12 and 1.35. While $\beta_{\rm B}$ was constrained by the BAT data themselves, we solved the coupled

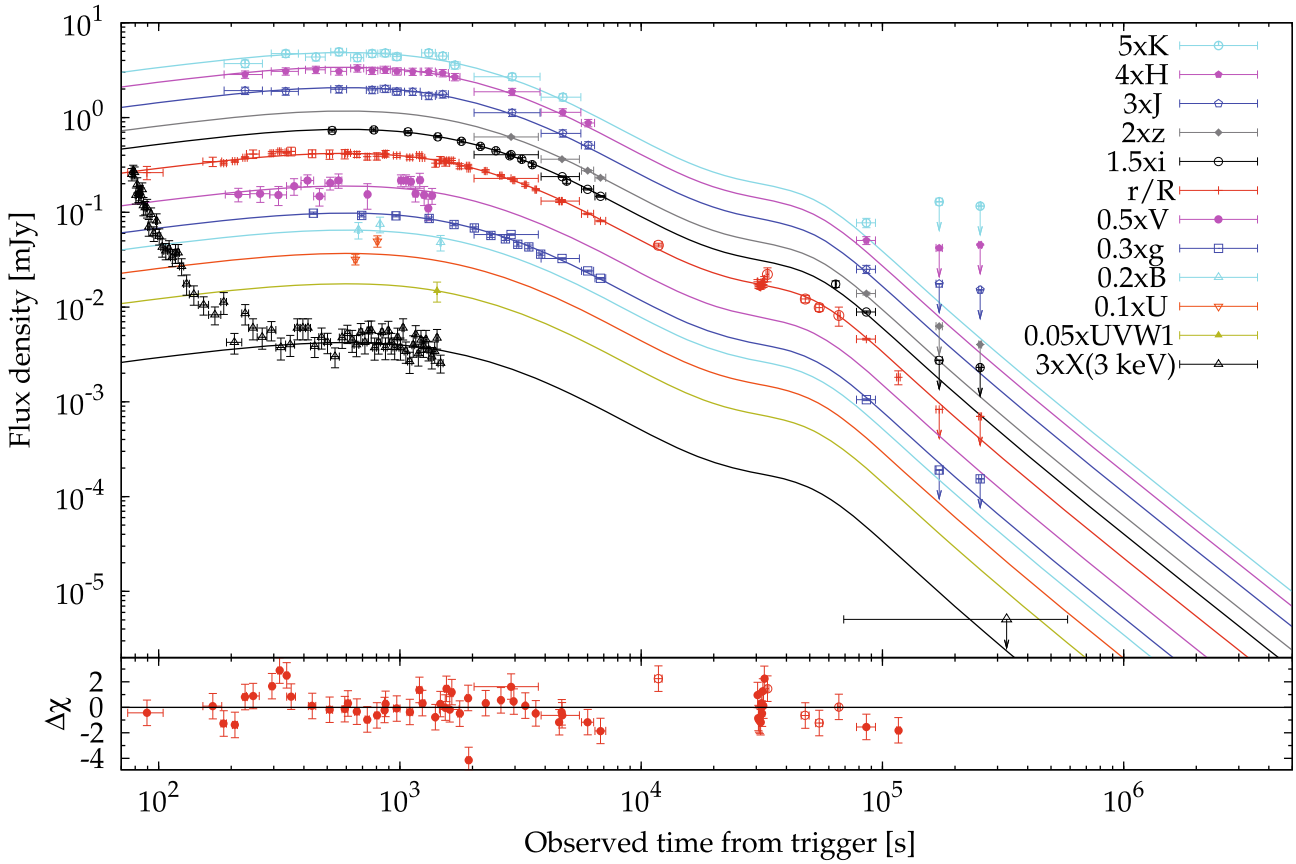

Fig. 5. *Top panel*: same as Fig. 4. In this case, the solid lines show the same model of a smoothly broken power-law plus a Lorentzian obtained by fitting all the curves simultaneously, allowing for different normalisations but with the same model fit parameters. *Bottom panel*: residuals of the r' curve with respect to the corresponding model.

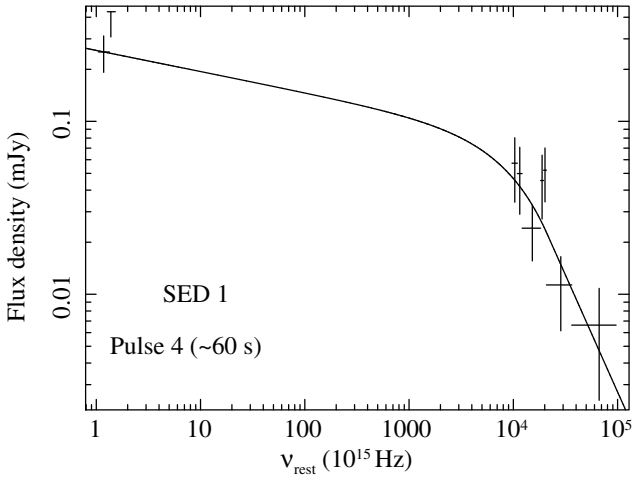

Fig. 6. GRB rest-frame SED 1 from observed optical to γ-ray during the optical flash concomitant with the last γ-ray pulse at ~60 s. The solid line shows the best-fit model smoothed broken power law (Band et al. 1993) with the following parameters: $\alpha_B = -1.1$, $\beta_B = -2.35$ and $E_{p,i} = 71$ keV.

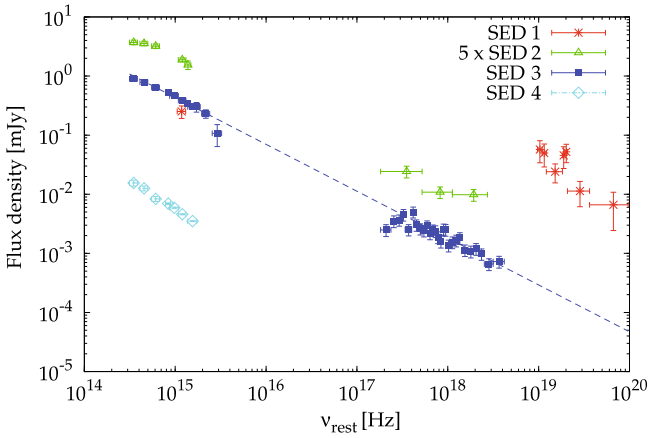

Fig. 7. GRB rest-frame SEDs 1 to 4 (shown with asterisks, triangles, squares, and diamonds, respectively). The dashed line shows the best-fit power-law model of SED 2: $\beta_{ox} = 0.79 \pm 0.01$ and $A_{V,z} < 0.02$. X-ray data were not absorption-corrected.

indetermination α_B–$E_{p,i}$ by initially freezing the low-energy index α_B to the typical value of -1 (Kaneko et al. 2006) and then allowing it to vary. The above minimum χ^2 was derived in this way. Although this does not break the degeneracy of both parameters (for every $E_{p,i} < 88$ keV there is a value of α_B for which an acceptable fit is given), here it is shown that the extrapolation of a typical Band model fitting the spectrum of the last pulse matches the optical flux observed during the flash. However, because of the lack of measurement of α_B from γ-ray data, the optical flux matched by the extrapolation of the Band model may still be accidental.

The time interval of SED 2 corresponds to the first JHK GROND frames and spans from 186.8 to 269.4 s (see Fig. 3). It consists of contemporaneous $Vr'JHK$ frames as well as X-rays. The NIR-to-X SED 2 can be fitted with a single power-law with

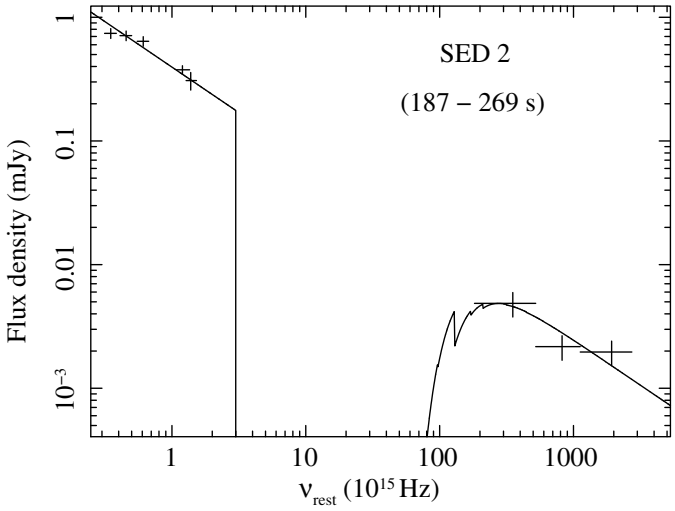

Fig. 8. GRB rest-frame SED 2 corresponding to the final part of the rise of the optical afterglow.

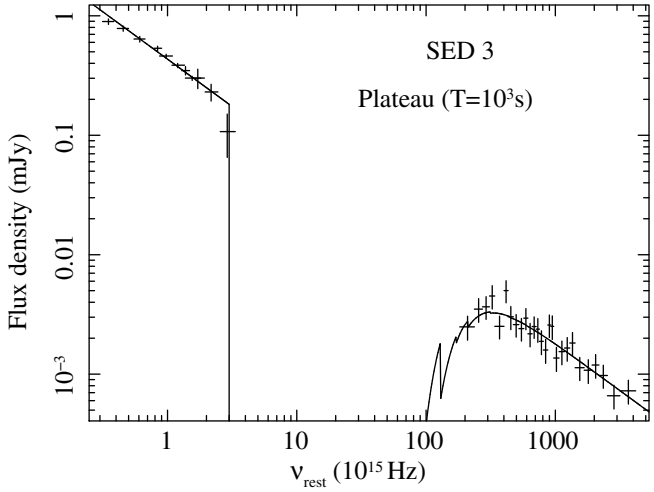

Fig. 9. GRB rest-frame SED from observed NIR to X-ray during the plateau from 400 to 1500 s. The solid line shows the best-fit model (SMC profile) corresponding to a single unextinguished power law with spectral index $\beta = 0.79 \pm 0.01$ and negligible local-frame extinction, $A_{V,z} < 0.02$ (see text).

$\beta_{ox} = 0.74 \pm 0.03$ and negligible dust extinction. The optical data alone can be fitted with an unextinguished power law with $\beta_o = 0.61 \pm 0.13$ (Table 2).

Taken during the plateau, SED 3 is the richest including all of the passband data considered in this work, apart from the γ-rays (see Fig. 3). Our NIR values are consistent with the JHK points of Bloom & Starr (2008). Given the steadiness of the light curve and evidence of no significant colour change along the plateau, the SED obtained in this way is fairly robust. The multiwavelength fitting of the light curves of Figs. 4 and 5 (Sect. 4.1) is dominated by data points along the plateau phase. Thus, we built a SED using the best-fit normalisations (Sects. 4.1.1 and 4.1.2) and calculated at the time of 10^3 s. We found the same results with improved uncertainties, due to the stronger constraints imposed by a multi-band fitting. The result of this SED is displayed in Fig. 9. The solid line shows the best-fit model obtained by adopting a rest-frame SMC-extinguished (Pei 1992), X-ray photoelectrically-absorbed power-law with $\beta_{ox} = 0.79 \pm 0.01$. We note that the point corresponding to the $UVW1$ filter agrees well with the Lyman absorption at the GRB redshift. The rest-frame optical extinction was found to be negligible and a very tight limit of $A_{V,z} < 0.02$ could be derived. Because of the more precise estimate obtained for β_{ox}, the estimate of $N_{H,z}$ improved correspondingly to $(2.7 \pm 0.8) \times 10^{21}$ cm^{-2}. These results are consistent with those obtained from the 0.3–10 keV spectrum alone and the accuracy of the estimates benefited significantly from the inclusion of NIR/visible data. Fitting the optical data alone, the result is similar: there is no need for a significant amount of extinction and, more importantly, the indices are equal, i.e., $\beta_o = \beta_{ox} = \beta_x$ (Table 2), which excludes the possibility of significant reddening due to dust along the line of sight within the host galaxy.

As a consequence, two properties are inferred:

- a negligible dust column-density in the circumburst environment and along the line of sight to the GRB through the host galaxy;
- a single power-law component accounting for the (observed) NIR to X-ray radiation, pointing to a single emission mechanism with no breaks in-between. Furthermore, a single power-law spectrum implies an achromatic evolution, which is consistent with the observations, while the converse is not true.

The epoch of SED 4 is ~80 ks, i.e., around the final break (aftermath of the late brightening) following the light-curve description given in Sect. 4.1.1 (Sect. 4.1.2) and shown in Fig. 4 (Fig. 5). This includes optical data and is shown in Fig. 7 (diamonds). Data can be fitted either with a single unextinguished power-law with $\beta_o = 1.05 \pm 0.06$ ($A_{V,z}$ fixed to 0) or, alternatively, with $\beta_o = 0.85 \pm 0.30$ and some extinction, $A_{V,z} = 0.10^{+0.14}_{-0.06}$. An increase in extinction with time seems difficult to explain physically, so we instead favour true reddening. Compared with the previous SEDs (Table 2), SED 4 is redder by $\Delta\beta_o = 0.26 \pm 0.06$ (significance of $\sim 6 \times 10^{-5}$). We point out that the reddening is independent of the fit choice, as demonstrated by comparing the power-law indices for no dust correction in the earlier and later spectra (Table 2).

5. Discussion

The 15–150 keV fluence and peak flux of XRF 080330 are typical of other XRFs detected by Swift. The X-ray afterglow flux places XRF 080330 in the low end of the distribution of the GRBs observed by Swift, which is similar to the majority of XRFs (Sakamoto et al. 2008). Moreover, the observed X-ray flux of XRF 080330 lies in the low end of both the XRFs sample of Swift considered by Sakamoto et al. (2008) and the XRFs sample of BeppoSAX of D'Alessio et al. (2006). The X-ray afterglow of XRF 080330 requires a remarkable steepening after the shallow phase with $\alpha_{x,3} > 1.3$, regardless of the light-curve modelling (Fig. 3). This decay is typical of classical GRBs (or steeper), but is in contrast to the fairly shallow decays found by Sakamoto et al. (2008) for their sample of Swift XRFs. The optical flux of the XRF 080330 afterglow is within 1σ of the distribution of the BeppoSAX XRFs sample of D'Alessio et al. (2006) at 40 ks post burst.

The coincidence of the steep decay observed in the X-ray light curve, which is a smooth continuation of the last γ-ray pulse, suggests that this corresponds to its high-latitude emission or the so-called "curvature effect" (Fenimore et al. 1996; Kumar & Panaitescu 2000; Dermer 2004). In the case of a thin shell emitting for a short time, the closure relation expected between temporal and spectral indices is $\alpha = \beta + 2$, the time origin

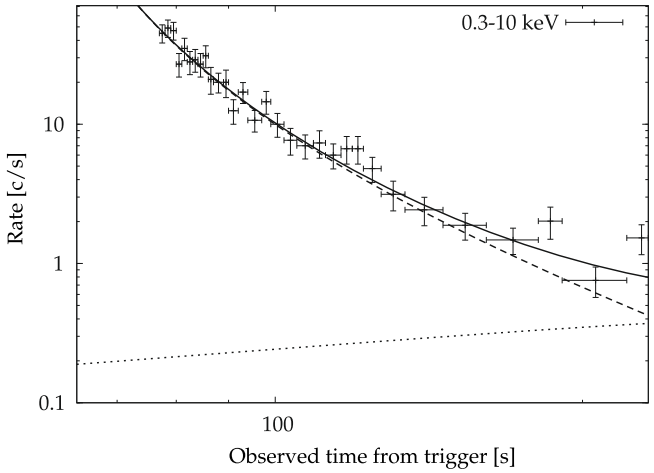

Fig. 10. 0.3–10 keV steep decay curve. The solid line shows the best-fitting model of the form $F(t)+k\,(t-t_0)^{-\alpha_x}$, where the parameters of $F(t)$ (Eq. (1)) were frozen to their best-fit values obtained by the multi-band fit of the afterglow component (Sect. 4.1.1) and with k, t_0 and α_x free parameters. Both terms, $F(t)$ and the power-law, are shown separately by the dotted and dashed curves, respectively.

t_0 being reset to the ejection time of the related pulse, earlier than the onset by about 3–4 times the width of the pulse. This still holds even if the emission occurs over a finite range of radii (Genet & Granot 2008), although in that case both the ratio of the ejection to pulse onset time difference and the pulse width become smaller ($\sim$1 for $\Delta R \sim R$).

We fitted the X-ray decay up to 210 s with the form $F(t) + k\,(t-t_0)^{-\alpha_x}$, where the parameters of $F(t)$ (Eq. (1)) were frozen to their corresponding best-fit model values obtained in Sect. 4.1.1, and the power-law parameters t_0, α_x and its normalisation k were left free to vary. We obtained $t_0 = 53^{+9}_{-18}$ s and $\alpha_x = 2.4^{+0.9}_{-0.5}$ s (χ^2/d.o.f. = 22/27), as shown by the solid line in Fig. 10. During the steep decay, it is $\beta_x = 1.06^{+0.10}_{-0.09}$ (Table 2). The curvature relation is fully satisfied and we note that t_0 corresponds to the time of the last pulse. Replacing Eq. (1) with Eq. (2) for the underlying component, $F(t)$, the best-fit parameters do not change by a noticeable degree.

The optical afterglow of XRF 080330 exhibited a slow rise up to $\sim$300 s, followed by a plateau to $\sim 2\times10^3$ s, after which it decayed with a typical power-law index of about 1.1 approximately out to a few 10^4 s. A sharp break to a decay index of $3.5^{+0.4}_{-0.3}$ then occurred concurrently with an optical reddening (Sect. 4.1.1; Fig. 4). Alternatively, after the plateau a more gradual transition to a power-law decay index of 2.0 ± 0.8 set in, followed by a smooth, red bump (Sect. 4.1.2; Fig. 5). We discuss each phase separately in the following subsections.

5.1. Optical afterglow rise

In the context of the fireball model (e.g., Mészáros (2006) and references therein), the possibility of the peak of the optical afterglow emission corresponding to the passage of the peak synchrotron frequency is excluded by the lack of spectral evolution: β_o should evolve from negative ($-1/3$) to positive values, while we find no evidence of β_o changing before $\sim 8\times10^4$ s.

Another possible interpretation of the optical peak is the onset of the afterglow, as for GRB 060418 and GRB 060607A (Molinari et al. 2007; Jin & Fan 2007) and, possibly, as well for XRF 071010A (Covino et al. 2008). In the case of XRF 080330, the rise during the pre-deceleration of the fireball within an ISM is much shallower than $\alpha \sim -3$, expected at frequencies between ν_m and ν_c (Sari & Piran 1999; Granot 2005; Jin & Fan 2007). A wind environment would reproduce the slow rise of XRF 080330 in a more effective way. With these assumptions and in the thin shell case since the GRB duration is much shorter than the deceleration time, we can estimate the initial Lorentz factor, Γ_0 (approximately, twice as large as the Lorentz factor at the peak), in a wind-shaped density profile, $n(r) = A\,r^{-s}$ (A is constant), with $s = 2$, from the peak time and the γ-ray radiated energy, E_{iso} (Chevalier & Li 2000; Molinari et al. 2007). For consistency, only the two-component model (Sect. 4.1.2; Fig. 5) must be considered. In this case, we take the peak time of the first component, $t_{p1} = 600$ s: assuming $\eta = 0.2$ (radiative efficiency), and $A = 3\times10^{35}$ cm^{-1}, it turns out that $\Gamma_0 < 80$, and a corresponding deceleration radius is smaller than 7×10^{16} cm. As in the case of XRF 071010A, the initial Lorentz factor is lower than those found for classical GRBs. There is no evidence of a reverse shock; if the injection frequency of the reverse shock occurred within the optical passbands, it would dominate the optical flux and exhibit a fast ($\sim t^{-2.1}$) decay (Kobayashi & Zhang 2007), which is not observed here. Nonetheless, this can still be the case if the injection frequency lies below the optical bands (Jin & Fan 2007; Mundell et al. 2007). A weak point of this interpretation is that the case $s = 2$ is ruled out: $\alpha = s(p+5)/4 - 3 = 0.79 \pm 0.01$ (Granot 2005). Inverting this relation, a value of $s = 1.4 \pm 0.1$ is required to explain the observed $\alpha = -0.4 \pm 0.2$. This argument, together with the absence of a reverse shock, whose $F_{\nu,max}$ should be much higher than that of the forward shock by a factor of $\sim\Gamma$ (although see above), makes the interpretation of a deceleration through a wind environment somewhat contrived.

For a single jet viewed off-axis (Granot et al. 2005), the rising part of the XRF 080330 curve is explained by the emission originating in the edge of the jet: as the bulk Lorentz factor Γ decreases, the beaming cone becomes progressively wider, resulting in a rising flux. The peak in the light curve is reached when it is $\Gamma \sim 1/(\theta_{obs} - \theta_0)$, where θ_{obs} and θ_0 are the viewing and jet opening angles, respectively. According to the optical afterglow classification given by Panaitescu & Vestrand (2008), XRF 080330 belongs to the class of slow-rising and peaking after 100 s events. Those authors found a possible anticorrelation between the peak flux and the peak time for a number of fast-rising afterglows, followed also by the slow-rising class and, in this respect, XRF 080330 is no exception. The suggested interpretation of the rise is either the pre-deceleration synchrotron emission or the emergence of a highly collimated outflow seen off-axis. In the latter case, assuming a power-law angular distribution of the kinetic energy, $\mathcal{E}(\theta) \propto (\theta/\theta_c)^{-q}$ ($q > 0$), high values for q correspond to slower rises and dimmer peak fluxes, for a fixed off-axis viewing angle ($\theta_{obs} = 2\,\theta_c$). In the former case, the anticorrelation is ascribed to different circumburst environment densities for different events: XRF 080330, because of the negligible dust extinction, would lie in the high-peak flux region, which is not the case. This favours the interpretation of an off-axis jet whose angular distribution of energy quickly drops away from the jet axis.

An example of another XRF whose optical counterpart showed a very similar behaviour is XRR 030418. The rise of this XRR, for which only an upper limit to its redshift ($z < 5$) was obtained (Dullighan et al. 2003), has been interpreted as being caused by the decrease in extinction with time, of the dust column density crossed by the fireball during its expansion (Rykoff et al. 2004). Figure 11 compares the light curve with that of XRF 080330. The solid line shows the best fit to the r' curve of XRF 080330 of Sect. 4.1.1, while the dashed line shows the

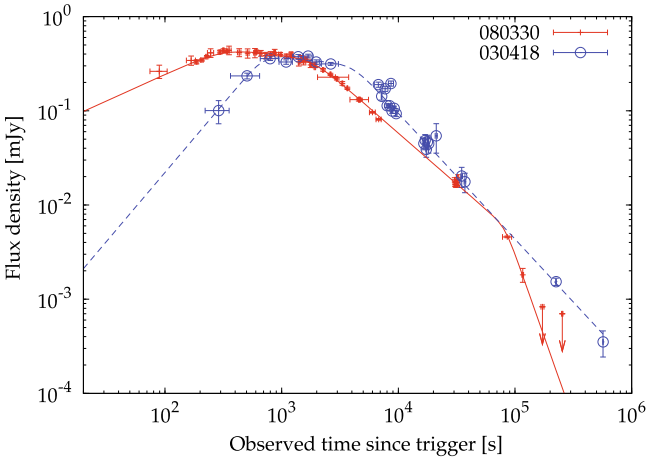

Fig. 11. r-band afterglow of XRF 080330 compared with the XRR 030418 (empty circles), for which there is only an upper limit to its redshift, $z < 5$ (Dullighan et al. 2003). Data of XRR 030418 have been taken from Rykoff et al. (2004); Ferrero et al. (2003); Dullighan et al. (2003). The solid line is the best fit of the XRF 080330 r curve of Sect. 4.1.1, while the dashed line is the best fit obtained with the same model applied to XRR 030418.

same model applied to the XRR 030418 data. XRR 030418 displays a steeper rise ($\alpha_1 = -1.5$), which strongly depends on the zero time and could be the same as that of XRF 080330 if the time origin was moved by (190 ± 50) s forward in time (lab frame). However, there is nothing around this time in the γ-ray light curve of XRR 030418. Apart from the different slopes of the rise and the lack of a late-time steepening in the case of XRR 030418, the plateau and post-plateau decay look very similar. If both XRFs are caused by the same process, from the spectral (lack of) evolution XRF 080330 during the rise-plateau-initial decay phases we can rule out the decreasing dust column-density hypothesis.

5.2. Plateau

From the SED extracted around the plateau no break is found between optical and X-ray frequencies, with $\beta_{ox} = 0.79 \pm 0.01$. In the regime of slow cooling, it is reasonable to assume that both optical (ν_o) and X-ray (ν_x) frequencies lie between the injection (ν_m) and the cooling (ν_c) frequencies, $\nu_m < \nu_o < \nu_x < \nu_c$ (Sari et al. 1998). The power-law index of the electron energy distribution, p, is given by $\beta_{ox} = (p-1)/2$, yielding $p = 2.58 \pm 0.02$, fully within the range of values found for other bursts (e.g., Starling et al. 2008). The temporal decay index depends on the density profile: the ISM (wind) case predicts a value of $\alpha = 3(p-1)/4 = 1.18 \pm 0.02$ ($\alpha = 3p/4 - 1/4 = 1.68 \pm 0.02$). After the plateau, depending on the light-curve modelling, the measured decay index is either $\alpha = \alpha_3 = 1.08 \pm 0.02$ (Sect. 4.1.1; Fig. 4) or $\alpha = \alpha_2 = 2.0 \pm 0.8$ (Sect. 4.1.2; Fig. 5). While the multiple smoothly broken power-law description (Sect. 4.1.1) definitely rules out the wind environment, both environments are still possible in the two-component model (Sect. 4.1.2), mainly because of the poorly measured decay index, α_2. If one interprets the flat decay as being due to energy injection (Nousek et al. 2006; Zhang et al. 2006), the corresponding index would be $q \sim 0.3$.

In the off-axis jet interpretation, even if we consider an initially uniform sharp-edged jet, the shocked external medium at the sides of the jet has a significantly smaller Lorentz factor than close to the head of the jet, and therefore its emission is not strongly beamed away from off-beam lines of sight. As a result, either an early very shallow rise or decay is expected for a realistic jet structure and dynamics (Eichler & Granot 2006). In the case of XRF 030723, Granot et al. (2005) showed that, for $\theta_{obs} \sim 2\,\theta_0$, an initial plateau is expected in the light curve.

Our observations of the afterglow rise of XRF 080330 exclude the interpretation proposed by Yamazaki (2009) of the plateau as being caused by an artifact of the choice of the reference time, as all the other rising curves do.

5.3. Jet break

According to the light-curve description of Sect. 4.1.1 shown in Fig. 4, for which only an ISM environment is possible (Sect. 5.2), after the plateau phase the light curve is expected to approach the on-axis light curve with $\alpha = 3(p-1)/4$. The late-time steepening observed around 8×10^4 s, estimated to be $\Delta\alpha = \alpha_4 - \alpha_3 = 2.4 \pm 0.4$, cannot be produced by the passage of the cooling frequency ν_c through the optical, which is expected to be as small as $\Delta\alpha = 1/4$ (ISM/wind).

In the off-axis jet interpretation, assuming a value for θ_0 of a few degrees, another advantage of this interpretation is the steep late-time decay (at $\gtrsim$1 day) caused by joining the post jet break on-axis light curve. According to the light-curve modelling given in Sect. 4.1.2 shown in Fig. 5, the gradual steepening following the plateau corresponds to the post-jet break emission: the observed power-law decay index, $\alpha_2 = 2.0 \pm 0.8$ is consistent with the expected value of $\alpha = p = 2.6$. We note that the relatively sharp jet break favours the ISM environment. Overall, in the context of an off-axis viewing angle interpretation, the light curve suggests that $\theta_{obs} \sim (1.5{-}2)\theta_0$ as well as an early jet break (at $\lesssim$1 day), which in turn implies a narrow jet with a half-opening angle of the order of a few degrees, $\theta_0 \sim 0.05$. As a simple feasibility check, we note that for $\theta_{obs} < 2\theta_0$ the ratio of the on-axis to off-axis $E_{\gamma,iso}$ is equal to δ^2 (assuming that the observed energy range includes E_p where most of the energy is radiated), where δ is the ratio of their corresponding Doppler factors and therefore of their E_p (Eichler & Levinson 2004). In our case, for an observed off-axis $(1+z)E_p \sim 60$ keV, an on-axis value of ∼1 MeV would require $\delta = 1 + [\Gamma_0(\theta_{obs} - \theta_0)]^2 \sim 17$ and $\Gamma_0(\theta_{obs} - \theta_0) \sim 4$, which for $\theta_{obs} - \theta_0 \sim (0.5{-}1)\theta_0$ and $\theta_0 \sim 0.05$ gives $\Gamma_0 \sim 80{-}160$. Here Γ_0 is the initial Lorentz factor at the edge of the jet. More realistically, the jet would not be perfectly uniform with extremely sharp edges, and instead Γ_0 is expected to be lower at the outer edge of the jet and higher close to its centre (where it could easily reach several hundreds in our illustrative example here). In this case, $\delta^2 \sim 300$ so that the observed $E_{\gamma,iso}$ in the 15−150 keV range, which is 2×10^{51} erg, would imply an on-axis value for $E_{\gamma,iso}$ of $\sim 10^{54}$ erg, which for a narrow jet with $\theta_{obs} \sim 0.05$ would correspond to a true energy of the order of 10^{51} erg. This demonstrates that this scenario can work for reasonable values of the physical parameters. We point out that the estimate of the on-axis $E_{\gamma,iso}$ of $\sim 10^{54}$ erg is for a wide energy range containing E_p, since in our illustrative example most of the energy is released within the observed range. A more accurate estimate of the break time and the corresponding opening angle is difficult, due to the degeneracy involved in the light-curve modelling (Figs. 4 and 5). Table 4 summarises the main properties of XRF 080330.

Table 4. Summary of the main properties of XRF 080330.

Name	Value
z	1.51
S(15–150 keV)	$(3.6 \pm 0.8) \times 10^{-7}$ erg cm^{-2}
P(15–150 keV)	(1.0 ± 0.2) ph cm^{-2} s^{-1}
$E_{\rm p}$	<35 keV
$E_{\rm p,i} = E_{\rm p}\,(1+z)$	<88 keV
$E_{\rm iso}$ (15–150 keV, obs frame)	$(2.1 \pm 0.5) \times 10^{51}$ erg
$E_{\rm iso}$ (1–10^4 keV, GRB frame)	$<2.2 \times 10^{52}$ erg
$t_{\rm jet}$ (obs frame)	$\lesssim$1 day
θ_0 (jet opening angle)[a]	few degrees
$\theta_{\rm obs}$ (viewing angle)[a]	$\sim(1.5-2)\theta_0$

[a] Under the assumption of a single off-axis jet.

Table 6. Lines detected in the XRF 080330 spectrum.

$\lambda_{\rm obs}$ [Å]	$\lambda_{\rm rest}$ [Å]	z	Feature	$EW_{\rm obs}$ [Å]
3889.4	1548.2/1550.8	1.5101	C IV	4.3 ± 0.7
4028.8	1608.5	1.5047	FeII	2.0 ± 0.7
4198.2	1670.8	1.5127	AlII	2.0 ± 0.7
5093.5	2026.1	1.5139	Zn II	4.3 ± 0.4
5190.3	2062.2	1.5166	CrII	0.6 ± 0.3
5190.3	2062.7	1.5166	ZnII	
5883.4	2344.2	1.5100	FeII	1.4 ± 0.5
5983.0	2382.8	1.5109	FeII	2.2 ± 0.5
6497.5	2586.7	1.51	FeII	11 ± 2
6527.0	2600.2	1.51	FeII	
7031.1	2796.3/2803.5	1.5112	MgII	5.2 ± 0.3

5.4. Late-time red bump

Overall, the two-component description of the light curves of Sect. 4.1.2 shown in Fig. 5 appears to be slightly more accurate than the multiple smoothly broken power-law of Fig. 4. So, irrespective of the nature of the rise and plateau, we speculate that the nature of the second component, modelled in Fig. 5, could be a late-time bump. Clearly, a SN bump, such as that possibly observed in the light curve of XRF 030723 (Fynbo et al. 2004), is ruled out mainly because that is expected to peak days later, which is incompatible with one single day after XRF 080330; not to mention the too high redshift of XRF 080330 for a 1998bw-like SN to be detected.

Alternatively, a density bump seems a viable solution, given that $\nu_{\rm o} < \nu_{\rm c}$ (e.g. Lazzati et al. 2002; Guidorzi et al. 2005), although the explanation of the observed contemporaneous reddening requires ad hoc assumptions, such as the case of GRB 050721, which showed similar properties to XRF 080330 (same $\beta_{\rm ox}$ with no breaks between optical and X-ray, and late-time redder optical bump). In that case, the observed reddening was explained as being due to the presence of very dense clumps surviving the GRB radiation and with a small covering factor (Antonelli et al. 2006).

If the late reddening is due to the passage of $\nu_{\rm c}$ through the optical bands, in addition to that argued in Sect. 5.3, another weak point of the multiple smoothly broken power-law description of Fig. 4 (Sect. 4.1.1) is the chromatic change of $\Delta\beta_{\rm o} = 0.26 \pm 0.06$ that we observe in the optical bands around 8×10^4 s. The passage of the cooling frequency does not explain this: the observed reddening would then be 0.5, i.e., twice as high. This could still be the case, if our measurement might have taken place in the course of the spectral change, because the broken power-law spectrum is a simple approximation. However, since $\nu_{\rm c} > \nu_{\rm x}$ during the plateau because of the unbroken power-law spectrum between optical and X-ray, $\nu_{\rm c}$ would have decreased very rapidly, implying that this option is unreasonable: if at 10^3 s, it is $\nu_{\rm c} > \nu_{\rm x} = 10^{18}$ Hz, at 10^5 s, it should be $\nu_{\rm c} > 10^{17}$ Hz $\gg \nu_{\rm o}$, because $\nu_{\rm c} \propto t^{-1/2}$ (ISM case), and this possibility is to be excluded. Likewise, in the wind case, it is $\nu_{\rm c} \propto t^{1/2}$. The times t_K and t_g, at which $\nu_{\rm c}$ would cross the most redward and blueward filters, K and g', would differ by a factor of $(\nu_g/\nu_K)^2 \sim 20$, which looks incompatible with the light curves. Furthermore, the observed reddening rules out the wind case, because $\beta_{\rm o}$ should decrease from $p/2$ to $(p-1)/2$.

Although an energy injection into the blast wave (forward shock) can explain the bump feature in the light curve, it is difficult to explain the reddening if we only consider the forward shock emission, as we have discussed. A possible explanation of the reddening is that the rebrightening is due to the short-lived ($\Delta t \sim t$) reverse shock of a slow shell caught up with the shock front and that increased its energy through a refreshed shock (e.g. Kumar & Panaitescu 2000; Granot et al. 2003; Jóhannesson et al. 2006): since that shock goes into a shell of ejecta, rather than the external medium, it can have a much higher value of ϵ_B (magnetised fireball: Zhang et al. 2003; Kumar & Panaitescu 2003; Gomboc et al. 2008b) and, therefore, a lower $\nu_{\rm c}$, quite naturally; for an ISM in which $\nu_{\rm c}$ decreases with time, $\nu_{\rm c}$ of the reverse shock could then be around the optical for reasonable model parameter values. The need for a separate component to explain a chromatic break in the light curve was also suggested in the case of GRB 061126 (Gomboc et al. 2008b). Notably, the final steepening after 10^5 s, which in the modelling of Sect. 4.1.1 (Fig. 4) is described with $\alpha_4 = 3.5^{+0.4}_{-0.3}$, is compatible with the high-latitude emission of the reverse shock: $\alpha = \beta_{\rm o,late} + 2 = 3.05 \pm 0.06$. The jet break might happen slightly earlier than the break time in the optical light curve.

A more contrived way to explain the bump is the appearance of a second narrower jet in the two-component jet model, as proposed for XRF 030723 (Huang et al. 2004). In this model, the viewing angle, is within or slightly off the cone of the wide jet and outside the narrow jet. The plateau phase would reflect the deceleration of the wide jet (Granot et al. 2006). Depending on the isotropic-equivalent kinetic energy of the wide and narrow jet, $E_{\rm w,iso}$ and $E_{\rm n,iso}$, on the jet opening angles, $\theta_{0,\rm w}$ and $\theta_{0,\rm n}$, on the initial bulk Lorentz factors, $\gamma_{0,\rm w}$ and $\gamma_{0,\rm n}$, respectively, as well as on the viewing angle, the afterglow emission of either component is dominant at different times. According to the results of Huang et al. (2004), the light curve of XRF 080330 could be qualitatively explained as follows: the first component obtained in Sect. 4.1.2 (Fig. 5) represents the contribution of the wide jet that dominates at early times: the rise could be due to either the afterglow onset (in a wind environment) or to a viewing angle slightly beyond the wide jet opening angle: $\theta_{\rm obs} \gtrsim \theta_{0,\rm w}$. The appearance of the second component would mark the deceleration and lateral expansion of the narrow jet, the peak time corresponding to the case $\gamma_{\rm n} \sim 1/\theta_{\rm obs}$. Unlike XRF 030723, which had a relatively sharp late-time peak, the bump exhibited by XRF 080330 looks less sharp and pronounced. Although this might suggest a relatively lower energy of the narrow jet compared to XRF 030723, we cannot exclude the case of $E_{\rm w,iso} \ll E_{\rm n,iso}$. The ratio of the observed energies of XRF 080330, of about 0.6 according to the modelling of Sect. 4.1.2, corresponds to the ratio of the early to the late time emissions of the wide and narrow jets, respectively. Depending on the values of $\theta_{\rm obs}$, $\theta_{0,\rm w}$, and $\theta_{0,\rm n}$, a comparable ratio of observed energies, such as that observed for XRF 080330, can still be obtained in the case of a far more energetic narrow jet, $E_{\rm w,iso} \ll E_{\rm n,iso}$. This model turned out to be successful in

accounting for the naked-eye GRB 080319B (Racusin et al. 2008): in that case, the two collimation-corrected energies were comparable, while the isotropic-equivalent energy of the narrow jet ($\theta_{0,n} = 0.2°$) was about 400 times higher than that of the wide jet ($\theta_{0,w} = 4.0°$).

However, for the two-component model the explanation of the late-time reddening simultaneously with the appearance of the narrow-component emission requires two different values of p for the two jets, which does not look reasonable on physical grounds. Another option is that the cooling frequency of the second jet might correspond to optical wavelengths at the time of the bump. However, if the shock microphysics parameters (p, ϵ_B, ϵ_e), are the same for the two shocks, as expected on physical grounds, and obviously the external medium is the same, then the only thing that differs as far as ν_c is concerned, is E_{iso}. Since the presence of the bump requires $E_{n,iso} > E_{w,iso}$, then this would not work for the wind case, where $\nu_c \propto E_{iso}^{1/2}$. Even in the ISM case, where $\nu_c \propto E_{iso}^{-1/2}$, since $\nu_c > \nu_x$ at 10^3 s, and therefore $\nu_c > 10^{17}$ Hz at 10^5 s for the wide jet, requires $E_{n,iso}/E_{w,iso} \gtrsim 10^4$ (which is very extreme) for $\nu_{c,n}(10^5$ s) to be around 10^{15} Hz (required by the observed reddening). Therefore, while this could work in principle, in practise it requires extreme parameters. In particular, the amplitude of the bump suggests that $E_n \sim E_w$, and therefore from the required $E_{n,iso}/E_{w,iso} \gtrsim 10^4$, it would follow that $\theta_n/\theta_w \lesssim 10^{-2}$, which seems incredible.

Overall, these considerations make the single off-axis jet interpretation far more compelling.

6. Conclusions

XRF 080330 is representative of the XRR and XRF classes of soft GRBs. Its γ- and X-ray properties of both prompt and high-energy afterglow emission place it at the low-flux end of the distribution. The multiband (NIR through UV) optical curve showed an initial rise up to ~300 s, followed by a ~2-ks long plateau, temporally coinciding with the canonical flat decay of X-ray afterglows of all kinds of GRBs, followed by a gradual steepening and a possible jet break. We provided two alternative descriptions of the light curve: a piecewise power law with three break times, the last of which occurred around 8×10^4 s, followed by a sharp steepening in which the power-law decay index changed from 1.1 to $3.5^{+0.4}_{-0.3}$. The SED from NIR to X-ray wavelength is fitted with a simple power-law with $\beta_{ox} = 0.8$ and negligible GRB-frame extinction, $A_V < 0.02$ adopting a SMC-like profile, with no evidence of chromatic evolution during the rise, plateau, and early ($<8 \times 10^4$ s) decay phases. However, after the possible late-time break we observe a reddening in the optical bands of $\Delta\beta_o = 0.26 \pm 0.06$, which cannot be accounted for in terms of the synchrotron spectrum evolution of a standard afterglow model, unless a different description of the light curve is considered. In the alternative model of the light curves, we identified two distinct components: the first is modelled with a smoothly broken power law and fits the rise plateau and early decay of the afterglow, while the second, considered around 8×10^4 s, is modelled with an energy-injection episode peaking at 34^{+11}_{-8} ks and with a time-integrated energy of ~60% that of the first component.

The X-ray light curve consists of the initial steep decay, which is likely the high-latitude emission of the last γ-ray pulse. At the same time, the optical afterglow rises up to a plateau, temporally coincident with the X-ray flat decay. In this case, we collected strong evidence that the emission mechanism during this phase is the same from optical to X-rays and is consistent with synchrotron emission of a decelerating fireball with an electron energy distribution power-law index of $p = 2.6$.

The lack of spectral evolution throughout the rise, plateau, and early decay argue against a temporally decreasing dust column-density, which has been claimed to explain similar optical light curves of past soft bursts. The optical rise ($\alpha \sim -0.4$) is too slow for the afterglow onset within a uniform circumburst medium, but could still be the case if a wind environment is considered. In this case, under standard assumptions we constrained the Lorentz factor of the fireball to be lower than 80, confirming the scenario predictions of XRFs as being less relativistic GRBs. However, we found that the interpretation of a single-component off-axis jet with an opening angle of a few degrees and a viewing angle about twice as large, can explain the observations: this not only accounts for the light curve morphology, but also explains the soft nature of XRF of the γ-ray prompt event. The reddening observed at 8×10^4 s can be interpreted as the short-lived reverse shock of an energy injection caused by a slow shell which caught up with the fireball shock front, also responsible for the contemporaneous bump in the light curve. A two-component jet could also work, but would introduce more free parameters and require extreme conditions.

The interpretation of the late bump being produced by a density enhancement in the medium swept up by the fireball cannot be ruled out, although the reddening seems to require ad hoc explanations. In this case, as shown by Nakar & Granot (2007), it is hard to produce a flux enhancement with density inhomogeneities, although it is not excluded given the lack of a sharp rise in this bump.

Overall, the XRF 080330 optical and X-ray afterglows properties have also been observed in many other GRBs (Panaitescu & Vestrand 2008). This both supports the view of a common origin of XRFs and classical GRBs, which form a continuum and do not require distinct mechanisms. The importance of a prompt multiwavelength coverage of the early phases of a GRB is clearly demonstrated in the case of XRF 080330.

Acknowledgements. This work is supported by ASI grant I/R/039/04 and by the Ministry of University and Research of Italy (PRIN 2005025417). J.G. gratefully acknowledges a Royal Society Wolfson Research Merit Award. DARK is funded by the DNRF. P.J. acknowledges support by a Marie Curie European Re-integration Grant within the 7th European Community Framework Program under contract number PERG03-GA-2008-226653, and a Grant of Excellence from the Icelandic Research Fund. We gratefully acknowledge the contribution of the Swift team members at OAB, PSU, UL, GSFC, ASDC, MSSL and our sub-contractors, who helped make this mission possible. We acknowledge Sami-Matias Niemi for executing the NOT observations. CG is grateful to A. Kann for his reading and comments.

References

Amati, L. 2006, MNRAS, 372, 233
Amati, L., Frontera, F., Tavani, M., et al. 2002, A&A, 390, 81
Amati, L., Frontera, F., in 't Zand, J. J. M., et al. 2004, A&A, 426, 415
Amati, L., Della Valle, M., Frontera, F., et al. 2007, A&A, 463, 913
Antonelli, L. A., Testa, V., Romano, P., et al. 2006, A&A, 456, 509
Band, D., Matteson, J., Ford, L., et al. 1993, ApJ, 413, 281
Barraud, C., Olive J.-F., Lestrade, J. P., et al. 2003, A&A, 400, 1021
Barthelmy, S. D., Barbier, L. M., Cummings, J. R., et al. 2005, Space Sci. Rev., 120, 143
Berger, E., Kulkarni, S. R., Pooley, G., et al. 2003, Nature, 426, 154
Bertin, E., & Arnouts, S. 1996, A&AS, 117, 393
Beuermann, K., Hessman, F. V., Reinsch, K., et al. 1999, A&A, 352, L26
Bloom, J. S., & Starr, D. L. 2008, GCN Circ., 7542
Burrows, D. N., Hill, J. E., Nousek, J. A., et al. 2005, Space Sci. Rev., 120, 165
Butler, N. R., Sakamoto, T., Suzuki, M., et al. 2005, ApJ, 621, 884
Campana, S., Mangano, V., Blustin, A. J., et al. 2006, Nature, 442, 1008
Cardelli, J. A., Clayton, G. C., & Mathis, J. S. 1989, ApJ, 345, 245

Chevalier, R. A., & Li, Z.-Y. 2000, ApJ, 536, 195
Clemens, C., Küpcü Yoldaş, A., Greiner, J., et al. 2008, GCN Circ., 7545
Cool, R. J., Eisenstein, D. J., Hogg, D. W., et al. 2008, GCN Circ., 7540
Covino, S., D'Avanzo, P., Klotz, A., et al. 2008, MNRAS, 388, 347
Cucchiara, A., & Fox, D. B. 2008, GCN Circ., 7547
D'Alessio, V., Piro, L., & Rossi, E. M. 2006, A&A, 460, 653
D'Avanzo, P., Covino, S., Fugazza, D., et al. 2008, GCN Circ., 7554
Della Valle, M., Chincarini, G., Panagia, N., et al. 2006, Nature, 444, 1050
De Pasquale, M., Oates, S. R., Page, M. J., et al. 2007, MNRAS, 377, 1638
Dermer, C. D. 2004, ApJ, 614, 284
Dermer, C. D., Chiang, J., & Mitman, K. E. 2000, ApJ, 537, 785
Devillard, N. 2001, ASP Conf. Ser., 238, 525
Donaghy, T. Q. 2006, ApJ, 645, 436
Dullighan, A., Butler, N. R., Ricker, G. R., et al. 2003, GCN Circ., 2236
Eichler, D., & Levinson, A. 2004, ApJ, 614, L13
Eichler, D., & Granot, J. 2006, ApJ, 641, L5
Fenimore, E. E., Madras, C. D., & Nayakshin, S. 1996, ApJ, 473, 998
Ferrero, P., Pizzichini, G., Bartolini, C., et al. 2003, GCN Circ., 2284
Fox, D. W., Yost, S. A., Kulkarni, S. R., et al. 2003, Nature, 422, 284
Frontera, F., Antonelli, L. A., Amati, L., et al. 2000, ApJ, 540, 697
Fukugita, M., Ichikawa, T., Gunn, J. E., et al. 1996, AJ, 111, 1748
Fynbo, J. P. U., Sollerman, J., Hjorth, J., et al. 2004, ApJ, 609, 962
Fynbo, J. P. U., Watson, D., Thöne, C., et al. 2006, Nature, 444, 1047
Gal-Yam, A., Fox, D. B., Price, P. A., et al. 2006, Nature, 444, 1053
Gehrels, N., Chincarini, G., Giommi, P. et al. 2004, ApJ, 611, 1005
Genet, F., & Granot, J. 2008, submitted [arXiv:0812.4677]
Genet, F., Daigne, F., & Mochkovitch, R. 2007, MNRAS, 381, 732
Ghirlanda, G., Ghisellini, G., & Lazzati, D. 2004, ApJ, 616, 331
Ghisellini, G., Ghirlanda, G., Nava, L., & Firmani, C. 2007, ApJ, 658, L75
Ghisellini, G., Nardini, M., Ghirlanda, G., & Celotti, A. 2009, MNRAS, 393, 253
Gomboc, A., Guidorzi, C., Mundell, C.G., et al. 2006, Il Nuovo Cimento B, 121, 1303
Gomboc, A., Guidorzi, C., Melandri, A., et al. 2008a, GCN Circ., 7539
Gomboc, A., Kobayashi, S., Guidorzi, C., et al. 2008b, ApJ, 687, 443
Granot, J. 2005, ApJ, 631, 1022
Granot, J., & Kumar, P. 2006, MNRAS, 366, L13
Granot, J., Panaitescu, A., Kumar, P., & Woosley, S. 2002, ApJ, 570, L61
Granot, Y., Nakar, E., & Piran, T. 2003, Nature, 426, 138
Granot, J., Ramirez-Ruiz, E., & Perna, R. 2005, ApJ, 630, 1003
Granot, J., Königl, A., & Piran, T. 2006, MNRAS, 370, 1946
Greiner, J., Bornemann, W., Clemens, C., et al. 2008, PASP, 120, 405
Guidorzi, C., Monfardini, A., Gomboc, A., et al. 2005, ApJ, 630, L121
Guidorzi, C., Monfardini, A., Gomboc, A., et al. 2006, PASP, 118, 288
Heise, J., in' t Zand, J., Kippen, R. M., & Woods, P. M. 2001, in Gamma-Ray Bursts in the Afterglow Era, ed. E. Costa, F. Frontera, & J. Hjorth (Berlin: Springer), 16
Huang, Y. F., Wu, X. F., Dai, Z. G., Ma, H. T., & Lu, T. 2004, ApJ, 605, 300
Im, M., Lee, I., Urata, Y., et al. 2008, GCN Circ., 7546
Ioka, K., Toma, K., Yamazaki, R., & Nakamura, T. 2006, A&A, 458, 7
Jóhannesson, G., Björnsson, G., & Gudmundsson, E. H. 2006, ApJ, 647, 1238
Jin, Z. P., & Fan, Y. Z. 2007, MNRAS, 378, 1043
Kalberla, P. M. W., Burton, W. B., Hartmann, D., et al. 2005, A&A, 440, 775
Kaneko, Y., Preece, R. D., Briggs, M. S., et al. 2006, ApJS, 166, 298
Klotz, A., Boër, M., & Atteia, J. L. 2008a, GCN Circ., 7536
Klotz, A., Boër, M., & Atteia, J. L. 2008b, GCN Circ., 7543
Klotz, A., Boër, M., Eysseric, J., et al., 2008c, PASP, 120, 1298
Kobayashi, S., & Zhang, B., 2007, ApJ, 655, 973
Krisciunas, K., Margon, B., & Szkody, P. 1998, PASP, 110, 1342
Kumar, P., & Piran, T. 2000, ApJ, 532, 286
Kumar, P., & Panaitescu, A. 2000, ApJ, 541, L51
Kumar, P., & Panaitescu, A. 2003, MNRAS, 346, 905
Landolt, A. U. 1992, AJ, 104, 340
Lazzati, D., Rossi, E., Covino, S., Ghisellini, G., & Malesani, D. 2002, A&A, 396, L5
Levan, A., Patel, S., Kouveliotou, C., et al. 2005, ApJ, 622, 977
Malesani, D., Fynbo, J. P. U., Jakobsson, P., & Vreeswijk, P. M. 2008, GCN Circ., 7544
Mangano, V., La Parola, V., Cusumano, G., et al. 2007, ApJ, 654, 403
Mao, J., & Guidorzi, C. 2008, GCN Circ., 7583
Mao, J., Baumgartner, W. H., Burrows, D. N., et al. 2008a, GCN Circ. 7537
Mao, J., Guidorzi, C., Markwardt, C., et al. 2008b, GCN Report, 132.1
Markwardt, C., Barthelmy, S. D., Cummings, J., et al. 2008, GCN Circ., 7549
Mészáros, P. 2006, Rep. Prog. Phys. 2006, 69, 2259
Mochkovitch, R., Daigne, F., Barraud, C., & Atteia, J.-L. 2004, ASP Conf. Ser., 312, 381
Molinari, E., Vergani, S. D., Malesani, D., et al. 2007, A&A, 469, L13
Morrison, R., & McCammon, D. 1983, ApJ, 270, 119
Moskvitin, A. S., Fatkhullin, T. A., Komarova, V. N., & Burenkov, A. N. 2008, GCN Circ., 7559
Mundell, C. G., Steele, I. A., Smith, R. J., et al. 2007, Science, 315, 1822
Nakar, E., & Granot, J. 2007, MNRAS, 380, 1744
Norris, J. P., Bonnell, J. T., Kazanas, D., et al. 2005, ApJ, 627, 324
Nousek, J. A., Koveliotou, C., Grupe, D., et al. 2006, ApJ, 642, 389
Panaitescu, A., & Vestrand, W. T. 2008, MNRAS, 387, 497
Pei, Y. C. 1992, ApJ, 395, 130
Peng, F., Königl, A., & Granot, J. 2005, ApJ, 626, 966
Pian, E., Mazzali, P., Masetti, N., et al. 2006, 442, Nature, 1011
Poole, T. S., Breeveld, A. A., Page, M. J., et al. 2008, MNRAS, 383, 627
Preece, R. D., Briggs, M. S., Pendleton, G. N., & Paciesas, W. S. 2000, ApJS, 126, 19
Racusin, J. L., Karpov, S. V., Sokolowski, M., et al. 2008, Nature, 455, 183
Roming, P. W. A., Kennedy, T. E., Mason, K. O., et al. 2005, Space Sci. Rev., 120, 95
Rykoff, E. S., Smith, D. A., Price, P. A., et al. 2004, ApJ, 601, 1013
Romano, P., Moretti, A., Banat, P. L. et al. 2006, A&A, 450, 59
Rossi, F., Guidorzi, C., Amati, L., et al. 2008, MNRAS, 388, 1284
Sakamoto, T., Lamb, D. Q., Kawai, N., et al. 2005, ApJ, 629, 311
Sakamoto, T., Hullinger, D., Sato, G., et al. 2008, ApJ, 679, 570
Sakamoto, T., Sato, G., Barbier, L., et al. 2009, ApJ, 693, 922
Salmonson, J. D. 2003, ApJ, 592, 1002
Sari, R., & Piran, T. 1999, ApJ, 520, 641
Sari, R., Piran, T., & Narayan, R. 1998, ApJ, 497, L17
Schaefer, B. E., & Guver, T. 2008, GCN Circ., 7538
Schlegel, D. J., Finkbeiner, D. P., & Davis, M. 1998, ApJ, 500, 525
Schubel, M., Reichart, D., Nysewander, M., et al. 2008, GCN Circ., 7560
Sergeev, A., Andreev, M., Petkov, V., Kurenya, A., & Pozanenko, A. 2008, GCN Circ., 7556
Shao, L., & Dai, Z. G. 2007, ApJ, 660, 1319
Starling, R. L. C., van der Horst, A. J., Rol, E., et al. 2008, ApJ, 672, 433
Tagliaferri, G., Goad, M., Chincarini, G., et al. 2005, Nature, 436, 985
Tominaga, N., Deng, J., Mazzali, P. A., et al. 2004, ApJ, 612, L105
Troja, E., Cusumano, G., O'Brien, P. T., et al. 2007, ApJ, 665, 599
Uhm, L. Z., & Beloborodov, A. M. 2007, ApJ, 665, L93
Wang, X. F., Li, J. Z., Feng, Q. C., et al. 2008, GCN Circ., 7550
Wren, J., Vestrand, W. T., Wozniak, P. R., & Davis, H. 2008, GCN Circ., 7568
Yamazaki, R. 2009, ApJ, 690, L118
Yamazaki, R., Ioka, K., & Nakamura, T. 2002, ApJ, 571, L31
Yuan, F., Rykoff, E. S., Schaefer, B. E., et al. 2008, in Nanjing Gamma-Ray Burst Conference, ed. Y.-F. Huang, Z.-G. Dai, & B. Zhang, AIP Conf. Proc., 1065, 103
Zhang, B. 2007, Chinese J. A&A, 7, 1
Zhang, B., Kobayashi, S., & Mészáros, P. 2003, ApJ, 595, 950
Zhang, B., Fan, Y. Z., Dyks, J., et al. 2006, ApJ, 642, 354
Zerbi, F. M., Chincarini, G., Ghisellini, G., et al. 2001, Astron. Nach., 322, 275

Table 5. Optical photometric set of XRF 080330.

Mid time (s)	Exposure (s)	Magnitude[a,b]	Filter	Telescope
438	30	17.68 ± 0.03	SDSS-*g*	LT
695	30	17.74 ± 0.04	SDSS-*g*	LT
963	60	17.75 ± 0.03	SDSS-*g*	LT
1323	60	17.82 ± 0.04	SDSS-*g*	LT
1677	60	17.98 ± 0.03	SDSS-*g*	LT
2036	60	18.07 ± 0.03	SDSS-*g*	LT
2385	60	18.27 ± 0.05	SDSS-*g*	LT
2737	60	18.36 ± 0.04	SDSS-*g*	LT
3081	60	18.50 ± 0.05	SDSS-*g*	LT
3426	60	18.57 ± 0.05	SDSS-*g*	LT
3832	120	18.76 ± 0.03	SDSS-*g*	LT
186	10	17.65 ± 0.05	SDSS-*r*	LT
207	10	17.60 ± 0.03	SDSS-*r*	LT
228	10	17.51 ± 0.03	SDSS-*r*	LT
295	10	17.39 ± 0.05	SDSS-*r*	LT
317	10	17.34 ± 0.04	SDSS-*r*	LT
339	10	17.37 ± 0.03	SDSS-*r*	LT
609	30	17.38 ± 0.04	SDSS-*r*	LT
864	30	17.43 ± 0.04	SDSS-*r*	LT
1204	60	17.44 ± 0.05	SDSS-*r*	LT
1559	60	17.58 ± 0.03	SDSS-*r*	LT
1918	60	17.72 ± 0.04	SDSS-*r*	LT
2268	60	17.86 ± 0.04	SDSS-*r*	LT
2622	60	17.98 ± 0.03	SDSS-*r*	LT
2967	60	18.10 ± 0.03	SDSS-*r*	LT
3312	60	18.22 ± 0.05	SDSS-*r*	LT
3659	60	18.35 ± 0.03	SDSS-*r*	LT
4579	3 × 10	18.65 ± 0.04	SDSS-*r*	LT
4688	30	18.65 ± 0.04	SDSS-*r*	LT
30 383	200	20.78 ± 0.06	SDSS-*r*	FTN
30 605	200	20.89 ± 0.06	SDSS-*r*	FTN
30 828	200	20.90 ± 0.06	SDSS-*r*	FTN
31 050	200	20.91 ± 0.06	SDSS-*r*	FTN
31 271	200	20.92 ± 0.06	SDSS-*r*	FTN
31 494	200	20.84 ± 0.06	SDSS-*r*	FTN
31 717	200	20.89 ± 0.06	SDSS-*r*	FTN
31 940	200	20.79 ± 0.06	SDSS-*r*	FTN
32 163	200	20.86 ± 0.07	SDSS-*r*	FTN
32 385	200	20.71 ± 0.07	SDSS-*r*	FTN
116 557	20 × 200	23.3 ± 0.2	SDSS-*r*	FTN
523	30	17.22 ± 0.04	SDSS-*i*	LT
779	30	17.20 ± 0.05	SDSS-*i*	LT
1080	60	17.26 ± 0.04	SDSS-*i*	LT
1439	60	17.38 ± 0.03	SDSS-*i*	LT
1799	60	17.50 ± 0.04	SDSS-*i*	LT
2155	60	17.64 ± 0.05	SDSS-*i*	LT
2503	60	17.75 ± 0.03	SDSS-*i*	LT
2850	60	17.88 ± 0.04	SDSS-*i*	LT
3195	60	17.98 ± 0.05	SDSS-*i*	LT
3540	60	18.12 ± 0.05	SDSS-*i*	LT
4908	30	18.56 ± 0.05	SDSS-*i*	LT
64 063	4 × 150	21.27 ± 0.09	SDSS-*i*	LT
120 821	10 × 200	>21.0	SDSS-*i*	FTN
2890	1476	18.24 ± 0.02	SDSS-*g*	GROND
4699	1414	18.88 ± 0.02	SDSS-*g*	GROND
6006	459	19.20 ± 0.02	SDSS-*g*	GROND
6786	459	19.40 ± 0.02	SDSS-*g*	GROND
85 843	11 522	22.60 ± 0.02	SDSS-*g*	GROND
171 989	5866	>24.46	SDSS-*g*	GROND
254 165	5655	>24.69	SDSS-*g*	GROND

Table 5. continued.

Mid time (s)	Exposure (s)	Magnitude[a,b]	Filter	Telescope
2890	1476	18.05 ± 0.02	SDSS-*r*	GROND
4699	1414	18.65 ± 0.02	SDSS-*r*	GROND
6006	459	18.99 ± 0.02	SDSS-*r*	GROND
67 86	459	19.18 ± 0.02	SDSS-*r*	GROND
85 843	11 522	22.29 ± 0.02	SDSS-*r*	GROND
171 989	5866	>24.15	SDSS-*r*	GROND
254 165	5655	>24.33	SDSS-*r*	GROND
2890	1476	17.86 ± 0.02	SDSS-*i*	GROND
4699	1414	18.43 ± 0.02	SDSS-*i*	GROND
6006	459	18.77 ± 0.02	SDSS-*i*	GROND
6786	459	18.95 ± 0.02	SDSS-*i*	GROND
85 843	11 522	22.00 ± 0.03	SDSS-*i*	GROND
171 989	5866	>23.28	SDSS-*i*	GROND
254 165	5655	>23.47	SDSS-*i*	GROND
2890	1476	17.69 ± 0.02	SDSS-*z*	GROND
4699	1414	18.27 ± 0.02	SDSS-*z*	GROND
6006	459	18.58 ± 0.02	SDSS-*z*	GROND
6786	459	18.77 ± 0.03	SDSS-*z*	GROND
85 843	11 522	21.82 ± 0.04	SDSS-*z*	GROND
171 989	5866	>22.68	SDSS-*z*	GROND
254 165	5655	>23.16	SDSS-*z*	GROND
228	60	16.90 ± 0.10	$J^{(c)}$	GROND
336	60	16.92 ± 0.10	$J^{(c)}$	GROND
559	60	16.86 ± 0.10	$J^{(c)}$	GROND
768	60	16.88 ± 0.10	$J^{(c)}$	GROND
871	60	16.85 ± 0.10	$J^{(c)}$	GROND
972	60	16.92 ± 0.10	$J^{(c)}$	GROND
1130	120	16.93 ± 0.10	$J^{(c)}$	GROND
1317	120	17.04 ± 0.10	$J^{(c)}$	GROND
1504	120	17.00 ± 0.10	$J^{(c)}$	GROND
2920	1200	17.48 ± 0.10	$J^{(c)}$	GROND
4736	1200	18.02 ± 0.10	$J^{(c)}$	GROND
6034	950	18.34 ± 0.10	$J^{(c)}$	GROND
85 868	9960	21.61 ± 0.11	$J^{(c)}$	GROND
172 013	5160	>21.99	$J^{(c)}$	GROND
254 200	4800	>22.15	$J^{(c)}$	GROND
228	60	16.78 ± 0.10	$H^{(c)}$	GROND
336	60	16.70 ± 0.10	$H^{(c)}$	GROND
448	60	16.65 ± 0.10	$H^{(c)}$	GROND
559	60	16.70 ± 0.10	$H^{(c)}$	GROND
667	60	16.62 ± 0.10	$H^{(c)}$	GROND
768	60	16.68 ± 0.10	$H^{(c)}$	GROND
871	60	16.65 ± 0.10	$H^{(c)}$	GROND
972	60	16.70 ± 0.10	$H^{(c)}$	GROND
1130	120	16.70 ± 0.10	$H^{(c)}$	GROND
1317	120	16.70 ± 0.10	$H^{(c)}$	GROND
1504	120	16.74 ± 0.10	$H^{(c)}$	GROND
1690	120	16.85 ± 0.10	$H^{(c)}$	GROND
2920	1200	17.24 ± 0.10	$H^{(c)}$	GROND
4736	1200	17.78 ± 0.10	$H^{(c)}$	GROND
6034	950	18.06 ± 0.10	$H^{(c)}$	GROND
85 868	9960	21.16 ± 0.11	$H^{(c)}$	GROND
172 013	5160	>21.36	$H^{(c)}$	GROND
254 200	4800	>21.28	$H^{(c)}$	GROND
228	60	16.73 ± 0.10	$K^{(c)}$	GROND
336	60	16.47 ± 0.10	$K^{(c)}$	GROND

Table 5. continued.

Mid time (s)	Exposure (s)	Magnitude[a,b]	Filter	Telescope
448	60	16.56 ± 0.10	$K^{(c)}$	GROND
559	60	16.42 ± 0.10	$K^{(c)}$	GROND
667	60	16.57 ± 0.10	$K^{(c)}$	GROND
768	60	16.46 ± 0.10	$K^{(c)}$	GROND
871	60	16.45 ± 0.10	$K^{(c)}$	GROND
972	60	16.55 ± 0.10	$K^{(c)}$	GROND
1317	120	16.45 ± 0.10	$K^{(c)}$	GROND
1504	120	16.53 ± 0.10	$K^{(c)}$	GROND
1690	120	16.77 ± 0.10	$K^{(c)}$	GROND
2920	1200	17.08 ± 0.10	$K^{(c)}$	GROND
4736	1200	17.62 ± 0.10	$K^{(c)}$	GROND
85 868	9960	20.93 ± 0.13	$K^{(c)}$	GROND
172 013	5160	>20.37	$K^{(c)}$	GROND
254 200	4800	>20.49	$K^{(c)}$	GROND
1238	60	17.33 ± 0.02	*R*	NOT
1609	300	17.46 ± 0.01	*R*	NOT
1927	60	17.61 ± 0.01	*R*	NOT
89.4	30	17.90 ± 0.19	SDSS-*r* equivalent	REM
167.6	30	17.61 ± 0.13	SDSS-*r* equivalent	REM
246.2	30	17.41 ± 0.12	SDSS-*r* equivalent	REM
354.2	30	17.34 ± 0.12	SDSS-*r* equivalent	REM
432.9	30	17.40 ± 0.11	SDSS-*r* equivalent	REM
511.1	30	17.42 ± 0.13	SDSS-*r* equivalent	REM
590.5	30	17.41 ± 0.13	SDSS-*r* equivalent	REM
663.6	30	17.42 ± 0.08	SDSS-*r* equivalent	REM
732.7	30	17.48 ± 0.09	SDSS-*r* equivalent	REM
802.7	30	17.47 ± 0.10	SDSS-*r* equivalent	REM
871.8	30	17.40 ± 0.09	SDSS-*r* equivalent	REM
971.1	60	17.45 ± 0.05	SDSS-*r* equivalent	REM
1099.9	60	17.50 ± 0.06	SDSS-*r* equivalent	REM
1403.1	30	17.65 ± 0.11	SDSS-*r* equivalent	REM
1471.4	30	17.57 ± 0.10	SDSS-*r* equivalent	REM
1540.5	30	17.62 ± 0.11	SDSS-*r* equivalent	REM
1640.7	60	17.58 ± 0.06	SDSS-*r* equivalent	REM
1769.5	60	17.73 ± 0.07	SDSS-*r* equivalent	REM
50.4	60.0	>16.6	clear	TAROT
120.9	67.8	17.62 ± 0.60	clear	TAROT
194.1	66.6	17.38 ± 0.46	clear	TAROT
249.3	30.6	16.96 ± 0.40	clear	TAROT
332.7	89.4	17.17 ± 0.25	clear	TAROT
429.0	91.2	17.07 ± 0.20	clear	TAROT
528.7	90.0	16.83 ± 0.29	*R*	TAROT
626.4	90.0	16.83 ± 0.22	clear	TAROT
723.0	90.0	16.86 ± 0.22	clear	TAROT
927.0	90.0	17.52 ± 0.46	clear	TAROT
1023.9	89.4	17.15 ± 0.30	clear	TAROT
1123.9	90.0	17.00 ± 0.39	*R*	TAROT
1222.5	89.4	16.73 ± 0.21	clear	TAROT
1318.5	89.4	16.75 ± 0.25	clear	TAROT
1418.3	90.0	>16.8	*R*	TAROT
68	10	>17.38	*V*	UVOT
103	40	20.06 ± 0.397	white	UVOT
128	10	18.55 ± 0.20	white	UVOT
138	10	18.36 ± 0.44	white	UVOT
148	10	18.28 ± 0.39	white	UVOT
158	10	18.39 ± 0.43	white	UVOT
168	10	18.22 ± 0.38	white	UVOT
178	10	18.05 ± 0.32	white	UVOT
214	50	17.74 ± 0.19	*V*	UVOT
264	50	17.72 ± 0.22	*V*	UVOT

Table 5. continued.

Mid time (s)	Exposure (s)	Magnitude[a,b]	Filter	Telescope
314	50	17.75 ± 0.26	*V*	UVOT
364	50	17.52 ± 0.23	*V*	UVOT
414	50	17.37 ± 0.17	*V*	UVOT
464	50	17.79 ± 0.24	*V*	UVOT
514	50	17.44 ± 0.18	*V*	UVOT
557	36	17.37 ± 0.20	*V*	UVOT
629	20	>18.02	UVW1	UVOT
654	20	17.14 ± 0.16	*U*	UVOT
673	10	17.81 ± 0.23	*B*	UVOT
688	10	17.76 ± 0.14	white	UVOT
733	20	17.74 ± 0.34	*V*	UVOT
782	20	>18.04	UVW1	UVOT
788	172	>18.77	UVW2	UVOT
807	20	16.66 ± 0.17	*U*	UVOT
827	10	17.66 ± 0.22	*B*	UVOT
838	10	17.55 ± 0.12	white	UVOT
848	10	17.91 ± 0.15	white	UVOT
992	796	>18.55	UVM2	UVOT
1010	50	17.37 ± 0.17	*V*	UVOT
1060	50	17.37 ± 0.17	*V*	UVOT
1110	50	17.41 ± 0.17	*V*	UVOT
1160	50	17.72 ± 0.21	*V*	UVOT
1210	50	17.36 ± 0.21	*V*	UVOT
1260	50	17.75 ± 0.26	*V*	UVOT
1310	50	18.11 ± 0.29	*V*	UVOT
1360	51	17.77 ± 0.22	*V*	UVOT
1426	10	17.67 ± 0.29	UVW1	UVOT
1475	20	18.14 ± 0.22	*B*	UVOT
72 100	5887	>20.10	*V*	UVOT
307 644	47 917	>21.49	*B*	UVOT
307 940	47 715	>20.53	*V*	UVOT
307 583	47 956	>21.15	*U*	UVOT
307 483	48 074	>21.58	UVW1	UVOT
391 039	40 970	>23.32	white	UVOT

[a] Values are not corrected for Galactic extinction; [b] errors at the 68% confidence level and upper limits (3σ) are given; [c] *AB* magnitudes.